

*This article has been accepted for publication in Monthly Notices of the Royal Astronomical Society ©: 2018 The Authors. Published by Oxford University Press on behalf of the Royal Astronomical Society. All rights reserved.*

# A census of cool-core galaxy clusters in IllustrisTNG

David J. Barnes<sup>1,2,★</sup>, Mark Vogelsberger,<sup>1,†</sup> Rahul Kannan,<sup>1,3,‡</sup> Federico Marinacci<sup>1,4</sup>,  
 Rainer Weinberger,<sup>4</sup> Volker Springel,<sup>4,5,6</sup> Paul Torrey,<sup>1,§</sup> Annalisa Pillepich,<sup>7</sup>  
 Dylan Nelson,<sup>6</sup> Rüdiger Pakmor,<sup>4</sup> Jill Naiman,<sup>3</sup> Lars Hernquist<sup>3</sup> and  
 Michael McDonald<sup>1</sup>

<sup>1</sup>Department of Physics, Kavli Institute for Astrophysics and Space Research, Massachusetts Institute of Technology, Cambridge, MA 02139, USA

<sup>2</sup>Jodrell Bank Centre for Astrophysics, School of Physics and Astronomy, The University of Manchester, Manchester M13 9PL, UK

<sup>3</sup>Harvard–Smithsonian Center for Astrophysics, 60 Garden Street, Cambridge, MA 02138, USA

<sup>4</sup>Heidelberg Institute for Theoretical Studies, Schloss-Wolfsbrunnengasse 35, D-69118 Heidelberg, Germany

<sup>5</sup>Zentrum für Astronomie der Universität Heidelberg, ARI, Mönchhofstr. 12-14, D-69120 Heidelberg, Germany

<sup>6</sup>Max-Planck-Institut für Astrophysik, Karl-Schwarzschild-Str. 1, D-85741 Garching, Germany

<sup>7</sup>Max-Planck-Institut für Astronomie, Königstuhl 17, D-69117 Heidelberg, Germany

Accepted 2018 July 28. Received 2018 July 28; in original form 2017 October 20

## ABSTRACT

The thermodynamic structure of hot gas in galaxy clusters is sensitive to astrophysical processes and typically difficult to model with galaxy formation simulations. We explore the fraction of cool-core (CC) clusters in a large sample of 370 clusters from IllustrisTNG, examining six common CC definitions. IllustrisTNG produces continuous CC criteria distributions, the extremes of which are classified as CC and non-cool core (NCC), and the criteria are increasingly correlated for more massive clusters. At  $z = 0$ , the CC fractions for two criteria are in reasonable agreement with the observed fractions but the other four CC fractions are lower than observed. This result is partly driven by systematic differences between the simulated and observed gas fraction profiles. The simulated CC fractions with redshift show tentative agreement with the observed fractions, but linear fits demonstrate that the simulated evolution is steeper than observed. The conversion of CCs to NCCs appears to begin later and act more rapidly in the simulations. Examining the fraction of CCs and NCCs defined as relaxed we find no evidence that CCs are more relaxed, suggesting that mergers are not solely responsible for disrupting CCs. A comparison of the median thermodynamic profiles defined by different CC criteria shows that the extent to which they evolve in the cluster core is dependent on the CC criteria. We conclude that the thermodynamic structure of galaxy clusters in IllustrisTNG shares many similarities with observations, but achieving better agreement most likely requires modifications of the underlying galaxy formation model.

**Key words:** methods: numerical – galaxies: clusters: general – galaxies: clusters: intracluster medium – X-rays: galaxies: clusters.

## 1 INTRODUCTION

Galaxy clusters are the most massive collapsed structures at the current epoch; forming hierarchically under gravity via the accretion of matter and merging with other collapsed haloes. This formation process shock-heats the intracluster medium (ICM) to  $10^7$ – $10^8$  K, resulting in the emission of X-rays. Early X-ray obser-

vations of the ICM revealed that the cooling time in the cores of some clusters was significantly shorter than the Hubble time (Lea et al. 1973; Cowie & Binney 1977; Fabian & Nulsen 1977; Mathews & Bregman 1978). Clusters with short central cooling times are also associated with more relaxed morphologies and drops in central temperatures, reaching only a third of the virial temperature (Ikebe et al. 1997; Lewis, Stocke & Buote 2002; Peterson et al. 2003; Vikhlinin et al. 2005). These systems are known as cool-core (CC) clusters (Molendi & Pizzolato 2001).

The fraction of the cluster population that host a CC depends strongly on the method of sample selection, due to the so-called cool-core bias (Eckert, Molendi & Paltani 2011). CCs are associated with a strong peak in their X-ray surface brightness and a higher

\* E-mail: [djbarnes@mit.edu](mailto:djbarnes@mit.edu)

† Alfred P. Sloan Fellow.

‡ Einstein Fellow.

§ Hubble Fellow.

X-ray luminosity at fixed mass compared to non-cool-core (NCC) clusters, making them more easily detected in flux-limited X-ray samples. Hence, the fraction of CCs in X-ray samples is likely overestimated. For example,  $\approx 60$  per cent of 207 clusters detected with *Einstein*, over 59 per cent of 55 clusters observed with *ROSAT*, and 72 per cent of 64 clusters in the HIFLUGCS sample were found to host a CC (White, Jones & Forman 1997; Peres et al. 1998; Hudson et al. 2010). However, the success of Sunyaev–Zel’dovich (SZ) surveys (Hasselfield et al. 2013; Bleem et al. 2015; Planck Collaboration XXVII 2016) has enabled the collection of mass-limited samples that avoid cool-core bias (see Lin et al. 2015). Using the Planck SZ sample, Planck Collaboration XI (2011) found that 35 per cent of the sample hosted a CC, Rossetti et al. (2017) found a CC fraction of 29 per cent and Andrade-Santos et al. (2017) found that, depending on the defining criterion, 28–39 per cent of Planck clusters hosted a CC.

Observational results suggest that the properties of CCs have evolved little since  $z \sim 1.6$ . The central electron number density, entropy, and cooling time of CC clusters at low redshift are similar to their high-redshift counterparts (Cavagnolo et al. 2009; McDonald et al. 2013, 2017), suggesting that thermal equilibrium in the cluster core is established very early in its formation history. These results are consistent with the observation that the fraction of strong CCs, defined by cuspliness of the electron number density (Vikhlinin et al. 2007) or concentration of the surface brightness (Santos et al. 2008, 2010), decreases with increasing redshift. This is because the majority of the cluster volume evolves self-similarly around a CC, increasing in density and reducing the contrast to the core with increasing redshift (McDonald et al. 2017).

Reproducing the observed CC/NCC fractions in numerical simulations has been a significant challenge (Borgani & Kravtsov 2011). Idealized simulations have examined the physical processes in idealized CC set-ups (e.g. McCourt et al. 2012; Sharma et al. 2012; Gaspari 2015; Li et al. 2015), but have not reproduced how CCs form or how they are maintained in a cosmological setting. Cosmological simulations give conflicting results on CC formation and maintenance. Kay et al. (2007) found that almost all clusters hosted a CC at both  $z = 0$  and  $z = 1$ . Burns et al. (2008) also found that the fraction of CCs as a function of redshift was roughly constant, but that only  $\approx 15$  per cent of systems hosted a CC. The predicted fraction of CC clusters is inconsistent with the observed fraction and the lack of evolution in the fraction of CC systems is in tension with the mild evolution that is observed (e.g. McDonald et al. 2017). Early work also proposed that the difference between CCs and NCCs was driven by activity at high redshift ( $z > 1$ ), with significant early mergers (Burns et al. 2008) or preheating (McCarthy et al. 2008) resulting in the production of NCC clusters and late-time mergers being unable to turn a CC into an NCC (Poole et al. 2008). This is in contrast to more recent numerical work that has shown that late-time mergers are capable of destroying CCs (Rasia et al. 2015), with Hahn et al. (2017) advocating that the angular momentum of the merger is critical in determining whether the CC is disrupted. Rasia et al. (2015) argue that the lack of AGN feedback in early work, which leads to overcooling, made the cores too resilient to late-time mergers. In addition, the conflicting numerical results are further complicated by the use of different criteria when defining a CC cluster.

In this paper, we examine the fraction of CC and NCC galaxy clusters in the IllustrisTNG simulations, a follow-up to the Illustris project that contains an updated galaxy formation model and larger simulation volumes. Compared to previous theoretical work our study has the advantages of: being a significantly larger sample

of clusters than many previous studies; being at higher numerical resolution compared to many previous works; employing a state-of-the-art galaxy formation model that shows good agreement with observational results from dwarf galaxies to cluster scales. This enables us to study the fraction of clusters defined as CC and NCC for a variety of criteria commonly used in the literature. We examine the fraction of CC clusters produced by the IllustrisTNG model at  $z = 0$  and compare the criteria distributions to those from low-redshift observational samples (Cavagnolo et al. 2009; Andrade-Santos et al. 2017). We then study how the CC fraction evolves with redshift for different criteria and compare the fraction of CCs and NCCs defined as relaxed as a function of redshift. Finally, we examine how cluster cores evolve compared to the rest of the cluster volume by comparing the hot gas profiles at  $z = 0$  and  $z = 1$ .

The paper is structured as follows. In Section 2, we briefly describe the IllustrisTNG model and the simulation volume we use. We present the CC criteria that we use throughout this work in Section 3. In Section 4, we examine the criteria as a function of mass and the correlation between them. We then investigate how the CC fraction, defined by the different criteria, evolves with redshift and the fraction of CC systems that are defined as relaxed in Section 5. In Section 6, we study how the profiles of CCs evolve compared to NCCs. We then present our conclusions in Section 7.

## 2 NUMERICAL METHOD

IllustrisTNG (Marinacci et al. 2018; Naiman et al. 2018; Nelson et al. 2018; Pillepich et al. 2018b; Springel et al. 2018) is a follow-up project to the Illustris simulation (Genel et al. 2014; Vogelsberger et al. 2014a,b; Sijacki et al. 2015), which reproduces the galaxy size–mass relation (Genel et al. 2018) and the metallicity content of the ICM (Vogelsberger et al. 2018). The IllustrisTNG suite contains three simulation volumes, TNG50, TNG100, and TNG300, each at three different resolution levels (1, 2, and 3). All simulations use a cosmological model with parameters chosen in accordance with the Planck Collaboration XIII (2016) constraints:  $\Omega_m = 0.3089$ ,  $\Omega_b = 0.0486$ ,  $\Omega_\Lambda = 0.6911$ ,  $\sigma_8 = 0.8159$ ,  $H_0 = 100 h \text{ km s}^{-1} \text{ Mpc}^{-1} = 67.74 \text{ km s}^{-1} \text{ Mpc}^{-1}$ , and  $n_s = 0.9667$ .

In this work, we analyse the clusters that are present in the TNG300-1 periodic volume. The TNG300-1 volume has a side length of 302.6 Mpc and a dark matter and baryonic mass resolution of  $5.9 \times 10^7 M_\odot$  and  $1.1 \times 10^7 M_\odot$ , respectively. The collisionless particles, i.e. stars and dark matter, have a softening length of 1.48 kpc, which is comoving for  $z > 1$ , and a fixed physical length for  $z \leq 1$ . The gas cells employ an adaptive comoving softening length that reaches a minimum of 0.37 kpc. The simulation was performed with the moving-mesh code AREPO (Springel 2010), and evolved the magneto-hydrodynamics equations (Pakmor & Springel 2013). IllustrisTNG employs an updated version of the Illustris galaxy formation model (Vogelsberger et al. 2013, 2014a,b; Genel et al. 2014; Torrey et al. 2014), a comprehensive set of subgrid physical models that now include a new radio mode AGN feedback scheme (Weinberger et al. 2017a), a re-calibrated SN wind model and an extension to the chemical evolution scheme (Pillepich et al. 2018a) and refinements to the numerical scheme to improve the convergence properties (Pakmor et al. 2016).

Haloes were identified via a standard friends-of-friends (FoF) algorithm with a linking length of  $b = 0.2$  and substructures were identified using SUBFIND (Springel et al. 2001; Dolag et al. 2009). We analyse a mass-limited sample and select all haloes

**Table 1.** Table summarizing the criteria used throughout this work with the CC and MCC definitions.

Criterion	Notation	Aperture	CC limit	MCC limit
Central electron number density	$n_e$	$0.012 r_{500}$	$> 1.5 \times 10^{-2} \text{ cm}^{-3}$	$> 0.5 \times 10^{-2} \text{ cm}^{-3}$
Central cooling time	$t_{\text{cool}}$	$0.012 r_{500}$	$< 1 \text{ Gyr}$	$< 7.7 \text{ Gyr}$
Central entropy excess	$K_0$	–	$< 30 \text{ keV cm}^{-2}$	$< 60 \text{ keV cm}^{-2}$
Concentration parameter (physical)	$C_{\text{phys}}$	40.0, 400.0 kpc	$> 0.155$	$> 0.075$
Concentration parameter (scaled)	$C_{\text{scal}}$	0.15, $1.0 r_{500}$	$> 0.5$	$> 0.2$
Cuspiness parameter	$\alpha$	$0.04 r_{500}$	$> 0.75$	$> 0.5$

with  $M_{500} > 10^{13.75} M_{\odot}^1$  at each redshift. At  $z = 0$  ( $z = 1$ ) this yields a sample of 370 (77) clusters with a median mass of  $M_{500} = 8.8 \times 10^{13} M_{\odot}$  ( $M_{500} = 8.2 \times 10^{13} M_{\odot}$ ). X-ray luminosities,  $L_X$ , are computed using the Astrophysical Plasma Emission Code (APEC; Smith et al. 2001) via the PYATOMDB module with atomic data from ATOMDB v3.0.3 (last described in Foster et al. 2012). We compute mock X-ray spectra for each individual chemical element tracked by the simulation in the rest-frame energy band 0.05–100 keV for each gas cell, using its density, temperature, and metallicity. We then sum the spectra for the elements to produce an X-ray spectrum for each cell. X-ray luminosity within an aperture is then calculated by summing the spectra in the desired energy band for the gas cells that fall within the aperture, see Le Brun et al. (2014) and Barnes et al. (2017a) for further details. The luminosity within a 2D aperture is computed by collapsing the 3D positions of the gas cells along the  $z$ -axis and then summing the luminosities of all gas cells within the FoF group whose 2D position is within the aperture. We have explored the impact of collapsing the positions along different axes or using the median or mean value from the three different axes and find that it makes negligible difference to the CC criteria distributions presented throughout this work.

### 3 COOL-CORE CRITERIA

The literature contains many ways of defining a CC cluster and the fraction of clusters defined as CC depends on the chosen criterion and the sample selection. Observationally, the choice of criterion used will depend on the quality and resolution of the data, for example, the ability to extract a temperature profile. In this section, we define the CC criteria that we will consider in this work.<sup>2</sup> The thresholds for defining a cluster as CC or moderate cool core (MCC) for the different criteria are summarized in Table 1. When calculating the criteria we only include non-star-forming gas that is cooling (i.e. not being heated via supernovae or AGN feedback) and has a temperature  $T > 1.0 \times 10^6 \text{ K}$ .

The choice of halo centre can impact the recovered CC fraction and in this work we always centre on the cluster’s potential minimum. McDonald et al. (2013) demonstrated that for strong CC centring via the gas centroid or X-ray peak yields the same result. In addition, the observational sample of Cavagnolo et al. (2009) and Andrade-Santos et al. (2017) only centre using the X-ray peak. Therefore, for consistency we always select X-ray peak centred data when we have the choice.

<sup>1</sup>We define  $M_{500}$  as the mass enclosed within a sphere of radius  $r_{500}$  whose mean density is 500 times the critical density of the Universe at the cluster’s redshift.

<sup>2</sup>The thresholds for different CC criteria are taken from the references within each section.

#### 3.1 Central electron number density

A rapidly cooling core will be colder than its surrounding material and, therefore, must be denser than its surroundings in order to maintain pressure equilibrium. Observationally, the electron number density is extracted from the measured surface brightness profile and requires significantly fewer counts than other CC criteria, such as the cooling time. Following Hudson et al. (2010), we define a cluster as CC if the average density  $n_e(< 0.012 r_{500}) > 1.5 \times 10^{-2} \text{ cm}^{-3}$ . We choose to measure the quantity inside a 3D aperture of  $0.012 r_{500}$  to mimic observational apertures (e.g. Hudson et al. 2010; Andrade-Santos et al. 2017; McDonald et al. 2017). Those clusters with a central density in the range  $0.5 \times 10^{-2} < n_e(< 0.012 r_{500}) \leq 1.5 \times 10^{-2} \text{ cm}^{-3}$  are defined as MCC clusters and the remaining are defined as NCC.

#### 3.2 Central cooling time

Classically, clusters have been defined as CCs if the cooling time of their central region is short compared to the age of the Universe. Cooling time is defined as

$$t_{\text{cool}} = \frac{3(n_e + n_i)k_B T}{2n_e n_i \Lambda(T, Z)}, \quad (1)$$

where  $n_i$  is the ion number density,  $k_B$  is Boltzmann’s constant,  $T$  is the temperature of the gas, and  $\Lambda$  is the cooling function, which is a function of temperature and metallicity,  $Z$ . Mimicking observations, we measure the average cooling time inside a 3D aperture of  $r < 0.012 r_{500}$  (e.g. McDonald et al. 2013). We define those clusters with a cooling time less than 1 Gyr as CCs. A common definition of an NCC cluster is that its central cooling time is more than half the age of the Universe, hence at  $z = 0$   $t_{\text{cool}} \approx 7.7 \text{ Gyr}$ . However, at  $z = 1$  half the age of the Universe implies a cooling time  $t_{\text{cool}} \approx 2.9 \text{ Gyr}$ . Therefore, following McDonald et al. (2013) we set the threshold for clusters to be considered as MCCs to  $t_{\text{cool}} < 7.7 \text{ Gyr}$  at all redshifts to make the definition independent of redshift. McDonald et al. (2013) tested the impact of the different definitions and found it to be negligible. Those clusters with  $t_{\text{cool}} \geq 7.7 \text{ Gyr}$  are defined as NCCs.

#### 3.3 Central entropy excess

The central entropy excess of a cluster is another method of defining whether it is a CC or not. To measure the central entropy excess we follow the method of Cavagnolo et al. (2009). We first compute the 3D radial entropy profile using 50 radial bins in the range  $10^{-3} - 1.5 r_{500}$ , where the entropy  $K = k_B T n_e^{-2/3}$ . We then fit the entropy profile in the range  $0.01 - 1.0 r_{500}$  with a power law of the form

$$K(r) = K_0 + K_{100} \left( \frac{r}{100 \text{ kpc}} \right)^a, \quad (2)$$

where  $K_0$  is the excess entropy above the best-fitting power law,  $K_{100}$  is the normalization of the entropy at 100 kpc,  $\alpha$  is the power-law index, and  $r$  is the radial distance from the cluster's potential minimum. We then use  $K_0$  as the measure of the central entropy excess. We define CC clusters as those with  $K_0 < 30 \text{ keV cm}^2$ , MCCs as those in the range  $30 \leq K_0 < 60 \text{ keV cm}^2$  and the remaining as NCCs.

### 3.4 X-ray concentration parameter

As the X-ray emissivity is proportional to the gas density squared, and only weakly depends on temperature, CC clusters should have X-ray bright cores. Therefore, the ratio of the X-ray luminosity within the core compared to the luminosity within a larger aperture should clearly demonstrate the presence of a CC. First proposed by Santos et al. (2008), this criterion is commonly known as the concentration parameter. We define the concentration parameter as

$$C_{\text{phys}} = \frac{L_{\text{X}}^{\text{soft}}(r_p < 40 \text{ kpc})}{L_{\text{X}}^{\text{soft}}(r_p < 400 \text{ kpc})}, \quad (3)$$

where  $L_{\text{X}}^{\text{soft}}$  is the soft-band X-ray luminosity in the energy range 0.5–5.0 keV and  $r_p$  is the projected radial distance from the cluster's potential minimum. Those clusters with  $C_{\text{phys}} > 0.155$  are defined as CCs, those in the range  $0.075 < C_{\text{phys}} \leq 0.155$  as MCCs, and the rest as NCCs. We also consider the modification to this parameter proposed by Maughan et al. (2012), a scaled concentration parameter where the apertures are scaled by the cluster's characteristic radius  $r_{500}$ ,

$$C_{\text{scal}} = \frac{L_{\text{X}}^{\text{soft}}(r_p < 0.15r_{500})}{L_{\text{X}}^{\text{soft}}(r_p < r_{500})}. \quad (4)$$

For the scaled concentration parameter, we define CCs as those with  $C_{\text{scal}} > 0.5$ , MCCs as  $0.2 < C_{\text{scal}} \leq 0.5$ , and the rest as NCCs.

### 3.5 Cuspiness parameter

First proposed by Vikhlinin et al. (2007), the cuspiness of the electron number density profile is a common metric for defining CC clusters. Following the literature, we calculate the cuspiness parameter of the 3D density profile, computed using 50 radial bins in the range  $10^{-3} - 1.5 r_{500}$ , via

$$\alpha = - \left. \frac{d \log n_e(r)}{d \log r} \right|_{r=0.04r_{500}}. \quad (5)$$

We define CCs as those with  $\alpha > 0.75$ , MCCs in the range  $0.5 < \alpha \leq 0.75$ , and the remaining are classified as NCCs. We have used the CC threshold from Hudson et al. (2010) that is marginally higher than the  $\alpha > 0.7$  used in Vikhlinin et al. (2007), but this choice makes negligible difference to the results presented in this work.

Using these common CC criteria we now examine the fraction of CC clusters produced by the IllustrisTNG model at  $z = 0$ .

## 4 LOW-REDSHIFT COOL CORES

The limited volume of the TNG300 simulation means that the overlap in the mass distributions of the observed and simulated samples is limited, with the observed clusters being more massive on average than the simulated clusters. Therefore, here we split the sample in three mass bins: low-mass ( $M_{500} < 9 \times 10^{13} M_{\odot}$ ), intermediate-mass ( $9 \times 10^{13} \leq M_{500} < 2.0 \times 10^{14} M_{\odot}$ ), and high-mass ( $M_{500} \geq 2 \times 10^{14} M_{\odot}$ ), and compare the complete sample and

the high-mass sample to the observed CC fraction. At  $z = 0$ , the mass bins contain 191, 139, and 49 clusters and have median  $M_{500}$  values of  $6.9 \times 10^{13}$ ,  $1.2 \times 10^{14}$ , and  $2.7 \times 10^{14} M_{\odot}$ , respectively. To explore the dependence of the CC criteria on the total mass of the halo we fit a simple linear relation of the form

$$y = mx + c, \quad (6)$$

and we measure the scatter about the best fit for each mass bin via

$$\sigma_{\log_{10}} = \sqrt{\frac{1}{N} \sum_{i=1}^N \log_{10}(y_i) - \log_{10}(y_{\text{mod}})}^2}, \quad (7)$$

where  $N$  is the number of clusters in the sample,  $Y_i$  is the measured criterion value,  $Y_{\text{mod}}$  is the expected criterion value for a cluster with a given  $M_{500}$ , and we note that  $\sigma_{\ln} = \ln(10)\sigma_{\log_{10}}$ . The fit and scatter uncertainties are computed by bootstrapping the sample 10 000 times.

### 4.1 CC fractions

In Fig. 1, we plot the different CC criteria presented in Section 3 as a function of  $M_{500}$  at  $z = 0$ . Clusters that are defined as CC are denoted by blue triangles, MCCs as black circles, and NCCs as red squares. The CC metrics all produce continuous distributions with no obvious bimodality or dichotomy, suggesting that CC and NCC clusters are the two extremes of the same distribution. In Appendix A, we examine the impact of numerical resolution on the criteria distributions using the level 1 and level 2 resolutions of the TNG300 simulation, finding that numerical resolution has minimal impact on the criteria presented here. The CC fractions are summarized in Table 2.

In the upper left panel of Fig. 1, we plot the central electron number density as a function of  $M_{500}$ . The complete sample of clusters yields a CC fraction of  $14 \pm 2$  per cent, an MCC fraction of  $39 \pm 2$  per cent and an NCC fraction of  $46 \pm 2$  per cent. For the high-mass sample, we find an increased CC fraction of the  $35 \pm 6$  per cent. We compare to the observed central electron number densities of the clusters present in the *Planck* Early Sunyaev–Zel'dovich (ESZ) sample (Andrade-Santos et al. 2017). Selecting clusters with  $z < 0.25$ , the observed sample has a CC fraction of  $41 \pm 4$  per cent. Therefore, the CC fraction recovered for the high-mass sample is in reasonable agreement with the observed CC fraction. Fitting the criterion distribution with the linear relation given in equation (6), we find a slope  $m = 0.32 \pm 0.38$ , i.e. consistent with no mass dependence. However, measuring the scatter within each mass bin we find that the scatter increases significantly for the high-mass bin.

The central cooling time as a function of  $M_{500}$  is plotted in the upper centre panel of Fig. 1. Defining CCs via this criterion we find that  $12 \pm 2$  per cent of clusters are defined as CC for the complete sample. In contrast to the central electron number density, the high-mass bin has a CC fraction of  $6 \pm 4$  per cent, a factor 2 lower than the complete sample. We compare to the observed clusters that form the *ACCEPT* sample (Cavagnolo et al. 2009) with  $z < 0.25$ , noting that the median mass of the observed sample is more massive than the simulated sample. The observed clusters yield a CC fraction of  $52 \pm 4$  per cent. However, the *ACCEPT* clusters are taken from the *Chandra* archive and in effect form an X-ray-selected sample, which suffers from CC bias. Andrade-Santos et al. (2017) quantify the selection effects by assuming that the mass function and X-ray luminosity–mass relation are power laws. Using values from Vikhlinin et al. (2009a) and Vikhlinin et al. (2009b), they estimate that CCs are overrepresented by a factor of  $\sim 2.2$ . This reduces the

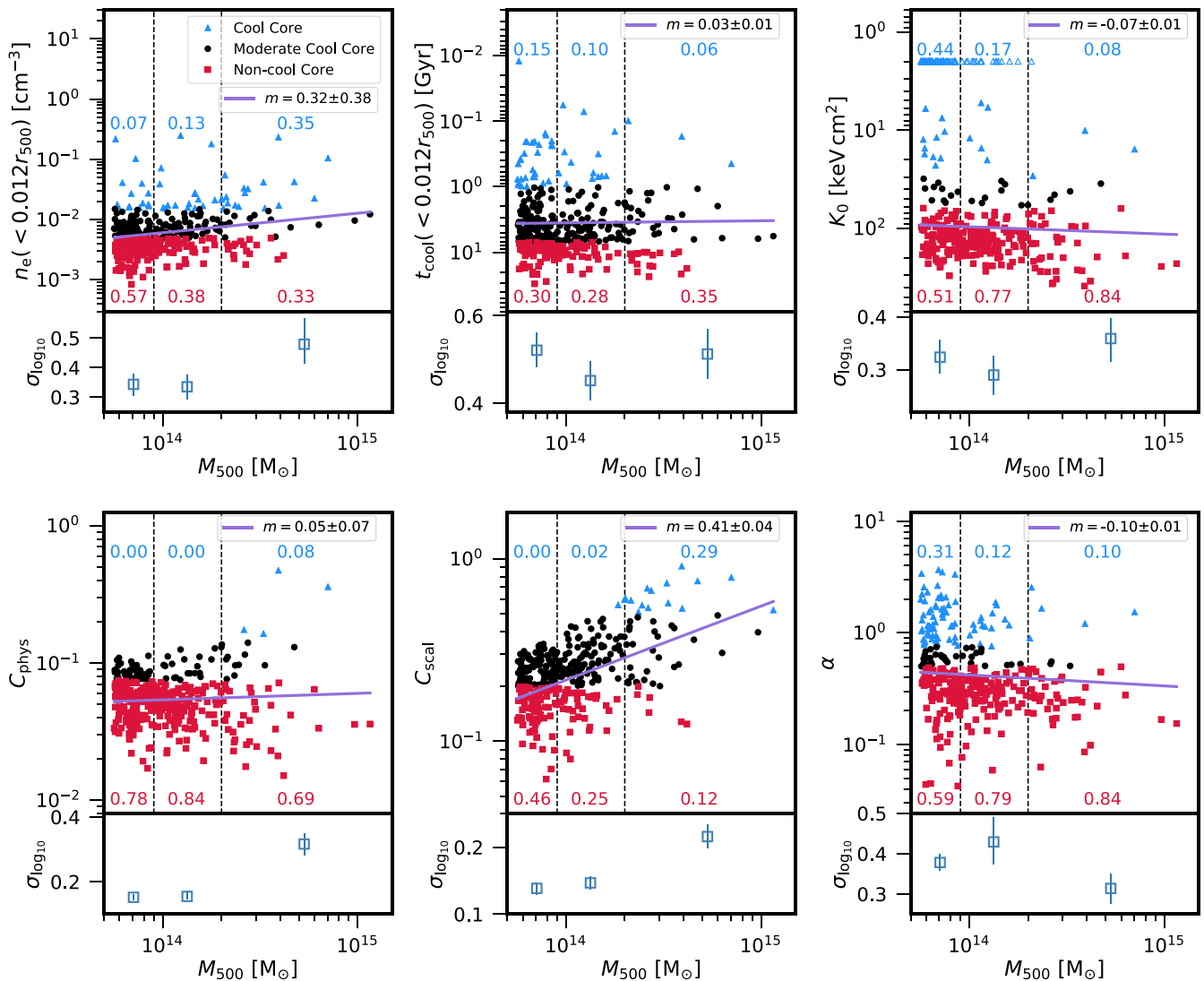


**Figure 1.** Comparison of the six CC criteria as a function of  $M_{500}$  at  $z = 0$  (upper panel) and the scatter relative to the best-fitting relation for the three mass bins (lower panel). We plot the central electron number density (top left), central cooling time (top centre), central entropy excess (top right), the concentration parameter within physical apertures (bottom left) and scaled apertures (bottom centre), and the cuspieness parameter (bottom right). CCs are denoted by blue triangles, MCCs by black circles, and NCCs by red squares. We set  $K_0 = 2 \text{ keV cm}^2$  for those clusters whose central entropy excess falls below this value, making them visible on the plot, and denote these systems by open symbols. The solid purple line denotes the best-fitting linear relation. The dashed black lines denote the mass bins and the (red) blue numbers give the fraction of (non-)cool-core systems in each bin. We note the y-axis is inverted for the central cooling time and central entropy excess, such that CCs always appear at the top of a panel.

observed CC fraction to 0.24 per cent, which is a factor 4 larger than CC fraction produced by the high-mass sample. Fitting the simulated criterion distribution as a function of mass we find a very weak mass dependence with a slope of  $m = 0.03 \pm 0.01$  and the scatter across the three mass bins is consistent within the errors.

CCs are defined by the central entropy excess in the upper right panel of Fig. 1. This yields a CC fraction of  $18 \pm 2$  per cent for the complete sample. Many of the simulated clusters defined as CC have very small central entropy excesses, which increases the simulated CC fraction and is further discussed below. To make these clusters visible on the plot we have set their central entropy excess to  $2 \text{ keV cm}^2$  and denoted them by open triangles. The central entropy excess produces a decreasing CC fraction with increasing halo mass with the high-mass bin yielding a CC fraction of  $10 \pm 6$  per cent, a factor 2 smaller than the observed CC fraction. For

the same CC definition clusters in the *ACCEPT* sample with  $z < 0.25$  yield a CC fraction of  $48 \pm 3$  per cent. However, we note that the limited resolution of the temperature profiles for some *ACCEPT* clusters have been shown to induce an artificial floor in the entropy profile (e.g. Panagoulia, Fabian & Sanders 2014; Hogan et al. 2017). This leads to a second peak in the entropy excess distribution at 15–20 keV. However, the true central entropy excess of these clusters would be lower than this artificial floor and these clusters would still be defined as CCs if the floor was removed. In addition, this second peak is 50–100 per cent lower than our adopted CC threshold and we still classify these objects as CCs. However, the observed CC fraction should be viewed as a lower limit. Therefore, despite well-documented issues, we compare to *ACCEPT* sample as it provides a large-statistic observational data set. Assuming that CCs are overrepresented in this X-ray-selected

**Table 2.** Table of the fraction of clusters defined as CC, MCC, or NCC for the criteria presented in Section 3 for the complete sample and the different mass bins at  $z = 0$ . All errors are computed by bootstrap resampling 10 000 times.

Sample ( $z = 0$ )	Fraction	Criteria					
		$n_e$	$t_{\text{cool}}$	$K_0$	$C_{\text{phys}}$	$C_{\text{scal}}$	$\alpha$
Complete	CC	$0.14 \pm 0.02$	$0.12 \pm 0.02$	$0.18 \pm 0.02$	$0.01 \pm 0.01$	$0.04 \pm 0.01$	$0.21 \pm 0.02$
( $M_{500} > 10^{13.75} M_{\odot}$ )	MCC	$0.39 \pm 0.03$	$0.58 \pm 0.03$	$0.10 \pm 0.01$	$0.20 \pm 0.02$	$0.62 \pm 0.02$	$0.09 \pm 0.01$
$N = 370$	NCC	$0.46 \pm 0.02$	$0.30 \pm 0.03$	$0.72 \pm 0.02$	$0.79 \pm 0.02$	$0.34 \pm 0.03$	$0.70 \pm 0.02$
Low-mass	CC	$0.07 \pm 0.02$	$0.15 \pm 0.03$	$0.28 \pm 0.04$	$0.00 \pm 0.01$	$0.00 \pm 0.01$	$0.31 \pm 0.04$
( $M_{500} < 9.0 \times 10^{13} M_{\odot}$ )	MCC	$0.36 \pm 0.03$	$0.55 \pm 0.03$	$0.12 \pm 0.02$	$0.22 \pm 0.04$	$0.54 \pm 0.04$	$0.10 \pm 0.03$
$N = 191$	NCC	$0.57 \pm 0.04$	$0.30 \pm 0.04$	$0.60 \pm 0.04$	$0.78 \pm 0.03$	$0.46 \pm 0.04$	$0.59 \pm 0.04$
Intermediate-mass	CC	$0.13 \pm 0.03$	$0.10 \pm 0.02$	$0.05 \pm 0.03$	$0.00 \pm 0.01$	$0.02 \pm 0.02$	$0.12 \pm 0.03$
( $9.0 \times 10^{13} \leq M_{500} < 2.0 \times 10^{14} M_{\odot}$ )	MCC	$0.49 \pm 0.05$	$0.62 \pm 0.05$	$0.06 \pm 0.02$	$0.16 \pm 0.04$	$0.73 \pm 0.04$	$0.09 \pm 0.03$
$N = 130$	NCC	$0.38 \pm 0.05$	$0.28 \pm 0.05$	$0.88 \pm 0.02$	$0.84 \pm 0.03$	$0.25 \pm 0.04$	$0.79 \pm 0.03$
High-mass	CC	$0.35 \pm 0.06$	$0.06 \pm 0.04$	$0.10 \pm 0.06$	$0.08 \pm 0.06$	$0.29 \pm 0.06$	$0.10 \pm 0.06$
( $M_{500} \geq 2.0 \times 10^{14} M_{\odot}$ )	MCC	$0.33 \pm 0.06$	$0.59 \pm 0.06$	$0.14 \pm 0.06$	$0.22 \pm 0.06$	$0.59 \pm 0.06$	$0.06 \pm 0.05$
$N = 49$	NCC	$0.33 \pm 0.06$	$0.35 \pm 0.06$	$0.76 \pm 0.05$	$0.69 \pm 0.06$	$0.12 \pm 0.06$	$0.84 \pm 0.07$

observational sample by a factor 2.2 the observed CC fraction of 22 per cent, a factor 2 larger than the high-mass sample. However, we note that both the simulations and observations have significant shortcomings and this may impact the CC fractions presented here. We fit the simulated criterion distribution, excluding those clusters with  $K_0 < 2 \text{ keV cm}^2$ , and find a weak mass dependence with a slope of  $m = -0.07 \pm 0.01$  and a scatter that is consistent within the error across the mass bins.

In the left and central bottom panels of Fig. 1, we plot the concentration parameter within physical,  $C_{\text{phys}}$ , and scaled,  $C_{\text{scal}}$ , apertures as function of  $M_{500}$ , respectively. Measured within physical apertures the concentration parameter produces a CC fraction of  $1 \pm 1$  per cent for the complete sample, while within scaled apertures the complete sample yields a CC fraction of  $4 \pm 1$  per cent. The high-mass sample yields CC fractions of  $8 \pm 6$  per cent and  $29 \pm 6$  per cent for the physical and scaled concentration parameter, respectively. The clusters in the *Planck* ESZ sample with  $z < 0.25$  produce CC fractions  $36 \pm 5$  per cent and  $28 \pm 4$  per cent for the physical and scaled concentration parameter, respectively. The high-mass bin is a factor 4.5 lower than observed for the physical concentration parameter and consistent with the observations for the scaled concentration parameter. Fitting the simulated criteria distributions we find that the physical concentration parameter is consistent with no mass dependence  $m = 0.05 \pm 0.07$ , while the scaled concentration parameter yields a slope of  $m = 0.41 \pm 0.04$  and increases with increasing halo mass. The scatter for both criteria increases significantly in the high-mass bin relative to the other bins.

Finally, in the bottom right panel of Fig. 1 we plot the cusiness parameter,  $\alpha$ , as a function of  $M_{500}$ . The complete sample yields a CC fraction of  $21 \pm 2$  per cent, which is a factor 2 larger than the CC fraction recovered for the high-mass bin. The clusters with  $z < 0.25$  in the *Planck* ESZ sample yield a CC fraction of  $35 \pm 5$  per cent, a factor 3.5 larger than the high-mass sample. Fitting the simulated criterion distribution as a function of mass we find a mild negative mass dependence  $m = -0.10 \pm 0.01$  with increasing halo mass and the scatter in the high-mass bin decreases relative to the other two mass bins.

Compared to other recent numerical work with modern hydrodynamic solvers and more developed subgrid prescriptions, we find that IllustrisTNG yields similar CC fractions. Rasia et al. (2015) found at  $z = 0$  that 38 per cent (11/29) of clusters were classified as CC, defined by pseudo-entropy and a central entropy excess criterion of  $K_0 < 60 \text{ keV cm}^2$ . Although we do not calculate a pseudo-

entropy for our clusters, if we make the same cut based on the central entropy excess we find that  $28 \pm 5$  per cent of the complete sample at  $z = 0$  are classified as CCs. In comparison,  $57 \pm 4$  per cent of clusters with  $z < 0.25$  in the *ACCEPT* sample are defined as CC, corrected to 26 per cent assuming a CC bias correction factor of 2.2. Hahn et al. (2017) defined a cluster as CC if the central entropy excess measured at 40 kpc was  $K_0 < 40 \text{ keV cm}^2$ . They find that 40 per cent (4/10) of their clusters at low-redshift ( $z \leq 0.37$ ) are classified as CC. Making the same cut in the central entropy excess the complete sample produces a CC fraction of  $19 \pm 2$  per cent at  $z = 0$  and  $49 \pm 3$  per cent at  $z = 0.4$ . With the same criterion the *ACCEPT* cluster sample at  $z < 0.25$  yields a CC fraction of  $50 \pm 3$  per cent (23 per cent corrected). The C-EAGLE project (Bahé et al. 2017; Barnes et al. 2017b) resimulated 30 clusters using the state-of-the-art EAGLE galaxy formation model (Crain et al. 2015; Schaye et al. 2015), at a similar resolution to the TNG100 level-1 volume. However, the clusters had low-density, high-entropy cores compared to the REXCESS sample, making it unlikely that any of these clusters would be classified as CCs. The low-density, high-entropy cores were thought to be due to the AGN feedback being ineffective at high redshift, resulting in some overcooling, and too active at late times, increasing the central entropy of the clusters. In summary, we find that the IllustrisTNG model yields a sample of clusters that, in general, has a lower CC fraction than observed when compared to low-redshift SZ-selected samples, where the impact of observational selection effects are expected to be less than 1 per cent (Pipino & Pierpaoli 2010; McDonald et al. 2013; Lin et al. 2015). However, the simulated CC fractions are consistent with other recent numerical work.

## 4.2 Cumulative gas fractions

To further understand the lower fraction of CCs present in the IllustrisTNG volume we now examine the cumulative and differential gas fractions. In Fig. 2, we plot the median cumulative (left-hand panel) and differential (right-hand panel) gas fraction as a function of radius at  $z = 0$ . We compare to the observed profiles from Pratt et al. (2010) and Landry et al. (2013) for the cumulative and differential profiles respectively. These have median masses of  $M_{500} = 2.8 \times 10^{14} M_{\odot}$  and  $M_{500} = 5.4 \times 10^{14} M_{\odot}$ . We calculate the median simulated profile for those clusters with  $M_{500} > 2 \times 10^{14} M_{\odot}$ , which yields a sample with a median mass of  $M_{500} = 2.78 \times 10^{14} M_{\odot}$ . We note the observational sample is X-ray selected and includes several very strong CCs.

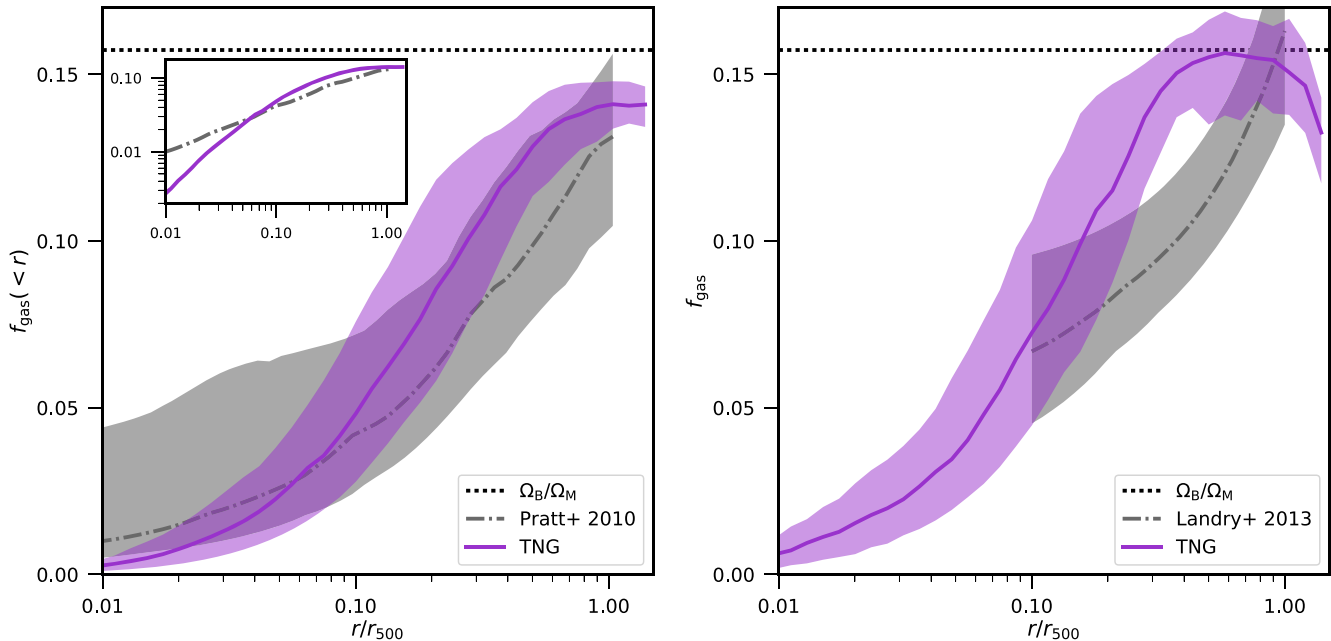


**Figure 2.** Median cumulative (left-hand panel) and differential (right-hand panel) gas fraction profiles as a function of  $r/r_{500}$  at  $z = 0$ . We plot the observed profiles from Pratt et al. (2010) and Landry et al. (2013, dashed grey line) for the cumulative and differential profiles, respectively, with the shaded regions encompassing 68 per cent of the sample. To ensure a fair comparison, we compute the median simulated profile for those clusters with  $M_{500} > 2 \times 10^{14} M_{\odot}$  (solid purple line). The universal baryon fraction  $f_b = (\Omega_B/\Omega_M \equiv 0.157)$  is denoted by the black dotted line. The inset in the left-hand panel shows the gas fraction profiles on a log scale to clarify the difference at small radii. The median simulated profiles rise more steeply than the observed profiles, before flattening at larger radii.

The observed cumulative median gas fraction increases by a factor of 3.1, from 28 per cent of the universal baryon fraction ( $\Omega_B/\Omega_M \equiv 0.157$ ) at  $0.1r_{500}$  to 83 per cent at  $r_{500}$ . Although the median simulated profile increases by a similar factor between  $0.1-1r_{500}$ , it rises more rapidly and reaches 86 per cent of the universal fraction at  $0.6r_{500}$ . Between  $0.6-1r_{500}$  the median profile flattens to a constant value of 90 per cent of the universal fraction. The simulated and observed differential profiles are similarly different, with the simulated profile rising much more rapidly than the observed profile and peaking at smaller radii compared to the observed profile. These differences between the observed and simulated profiles suggest that the simulated AGN feedback is more violent than in reality. This drives gas from the centre and results in a steepening of the gas fraction profiles, though we note that the feedback is significantly gentler than the previous Illustris model which removed the gas from the potential entirely (Genel et al. 2014). Additionally, the cumulative profiles show that the gas fraction within  $r_{500}$  is higher than observed by  $\sim 10$  per cent. This may indicate that the AGN is not efficient enough at removing gas from the potential at high redshift, and ejected gas then is reaccreted at low redshift. Similar gas fraction results were found in the C-EAGLE cluster simulations (Barnes et al. 2017b).

The gas fraction profiles help to explain why we find a lower simulated CC fraction than observed, especially for the concentration parameter. A gas fraction that rises more rapidly will result in a greater fraction of the X-ray emission coming from larger radii. This will result in systematically lower concentration parameter values. In the inset of Fig. 2 we plot the gas fraction on a log scale and we find that the median simulated gas mass enclosed in  $0.01r_{500}$  is 70 per cent lower than observed. Therefore, the central electron number density in the simulated clusters is systematically lower and fewer clusters will be defined as CCs by this criterion. From

equation (1), it is clear that a lower central number density will also produce longer cooling times and result in fewer clusters being defined as CCs by the cooling time criterion.

We examine the difference between the cumulative gas mass profiles for CCs and NCCs for the complete sample in Fig. 3, where CCs are defined by the central electron number density (left-hand panel), cooling time (middle panel), and cuspsiness parameter (right-hand panel) criteria. In general, we find that CC and NCC clusters have very similar profiles, regardless of defining criteria. This is in contrast to previous numerical work by Hahn et al. (2017), who found that their simulated CCs had significantly higher central gas fractions compared to NCCs, but in agreement with Eckert et al. (2013), who observed little difference between the CC and NCC gas fraction profiles of 62 clusters. Defining CCs by their central cooling time, the median profiles and the region denoting 68 per cent of the population are almost identical at all radii. Defining CCs by their central electron number density results in the CC profile having a higher median gas fraction at a fixed radius compared to the NCC median profile, 70 per cent at  $0.1r_{500}$ , and larger variation in the region denoting 68 per cent of the sample. This most likely reflects the inclusion of a greater fraction of more massive objects in the CC profile, as the CC fraction increases with increasing mass for this criterion. Defining CCs by the cuspsiness parameter results in the opposite trend, with NCC clusters having a marginally higher gas fractions at a fixed radius. The cuspsiness parameter has a decreasing CC fraction with increasing mass, and fewer massive clusters are included in the CC profile.

### 4.3 CC criteria distributions

We now compare the CC criteria distributions for the complete sample, the high-mass sample and the observational sample, which

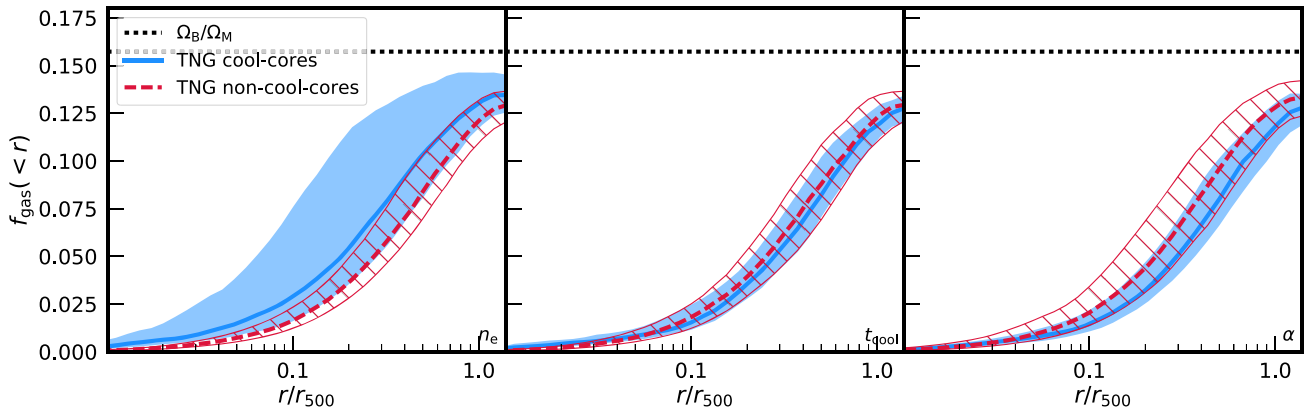


**Figure 3.** Median cumulative gas fractions at  $z = 0$  for CCs (solid blue line) and NCCs (red dashed line) defined by the central electron number density (left-hand panel), central cooling time (centre panel), and cuspsiness parameter (right-hand panel). The shaded (hashed) region denotes 68 per cent of the sample for CCs (NCCs) and the dotted line denotes the universal baryon fraction. We find that CCs and NCCs have very similar gas profiles regardless of the defining criterion.

are plotted in the diagonal panels of Fig. 4. For the central electron number density, the concentration parameters and the cuspsiness parameter we compare to *Planck* ESZ sample (Andrade-Santos et al. 2017) and for the central cooling time and central entropy excess we compare to the *ACCEPT* cluster sample (Cavagnolo et al. 2009). Excluding the observed central entropy excess distribution, we find both the observed and simulated distributions are reasonably well described by lognormal distributions. The observed central entropy distribution is clearly bimodal. However, as noted, previous work by Panagoulia et al. (2014), Hogan et al. (2017), and others have shown that the peak at  $15 \text{ keV cm}^2$  appears to be generated by the limited resolution of the temperature profiles, which complicates a direct comparison.

A sizable fraction of the simulated clusters have a very low central entropy excess ( $< 2 \text{ keV cm}^2$ ), which may suggest that physical processes are missing from the IllustrisTNG model. All cosmological simulations currently lack the resolution and the physics to correctly capture the multiphase nature of the ICM. Idealized simulations have shown a cluster’s entropy floor is set by the ratio of the cooling time to the free-fall time (Gaspari, Ruszkowski & Sharma 2012; McCourt et al. 2012; Sharma et al. 2012; Li & Bryan 2014). Once  $t_{\text{cool}}/t_{\text{ff}} \approx 10$ , cold gas begins to precipitate out of the hot gas, triggering AGN feedback events that maintain the central entropy. This result is supported by multiwavelength observations of filamentary molecular gas structures surrounding brightest cluster galaxies (BCGs; McDonald et al. 2010; McDonald, Veilleux & Mushotzky 2011; Werner et al. 2014; Tremblay et al. 2015; Suess et al. 2017). Cosmological simulations may need to model AGN triggering by cold phase precipitation to reproduce the minimum entropy floor. However, observations (e.g. Panagoulia et al. 2014) have shown that the entropy profiles are almost pure power laws at radii that are sufficiently well resolved, but the overall fraction of objects with these almost pure power-law profiles is uncertain as this study is X-ray selected and likely suffers from CC bias. If the clusters with negligible central entropy excess are removed, a comparison of the central entropy excess distributions for the complete and high-mass samples demonstrates that they are very similar, with mean values of  $179 \text{ keV cm}^2$  and  $176 \text{ keV cm}^2$  and standard deviations of  $\sigma = 0.42$  and  $\sigma = 0.52$  for the complete and high-mass samples, respectively.

The high-mass sample has significantly different central cooling time distribution compared to the observed distribution, but it

is similar to the complete sample distribution. The complete and high-mass distributions have mean values of 6.29 and 5.42 Gyr and standard deviations of  $\sigma = 0.63$  and  $\sigma = 0.86$ , respectively. In contrast, the observed distribution is very broad with a standard deviation of  $\sigma = 1.90$ . Although selection effects, which we do not account for, will impact the observed distribution, the central cooling time is a balance between radiative losses, thermal conduction and heating by feedback processes and merger events. Therefore, it is unlikely the simulations will be able to reproduce the observed distribution without accurately modelling all of these processes.

The complete and high-mass samples have similar mean values for the central electron number density criterion, with values of  $0.50 \times 10^{-2}$  and  $0.58 \times 10^{-2} \text{ cm}^{-3}$ , respectively. However, the high-mass sample has a larger standard deviation  $\sigma = 1.39$  compared to the complete sample  $\sigma = 0.97$  that is driven by a long tail towards higher central density values, producing the larger CC fraction. The observed sample has mean value of  $1.07 \times 10^{-2} \text{ cm}^{-3}$ , which is a factor 2 larger than the high-mass sample and has a standard deviation of  $\sigma = 1.13$ . Therefore, the observed CC fraction is likely  $1\sigma$  larger than the observed fraction because the mean value of the distribution is higher, which is likely a consequence of simulations having lower than observed central gas fractions.

The concentration parameter distributions are the most discrepant distributions for the complete and high-mass samples. Within physical apertures they have mean values of  $5.44 \times 10^{-2}$  and  $3.92 \times 10^{-2}$  and standard deviations of  $\sigma = 0.43$  and  $\sigma = 0.99$ , respectively. This compares to the observed distribution which has a mean value of  $4.33 \times 10^{-2}$  and a standard deviation of  $\sigma = 0.99$ . For the scaled concentration parameter, the complete and high-mass samples have mean values of 0.22 and 0.34 and standard deviations of  $\sigma = 0.42$  and  $\sigma = 0.52$ , respectively. The observed sample has a mean value of 0.51 and standard deviation of  $\sigma = 0.26$ . Therefore, although the high-mass sample has a lower mean value compared to the observed sample, the CC fraction is similar because the width of the high-mass sample distribution is larger.

The cuspsiness parameter distributions of the complete sample and the high-mass sample are marginally different. The complete sample has a mean value of 0.46 with a standard deviation of  $\sigma = 0.75$ , while the high-mass sample has a lower mean value of 0.27 and a similar standard deviation  $\sigma = 0.80$ . Therefore, the complete sample has a higher CC fraction because the mean value of the distribution is larger. However, the simulated cuspsiness parameter

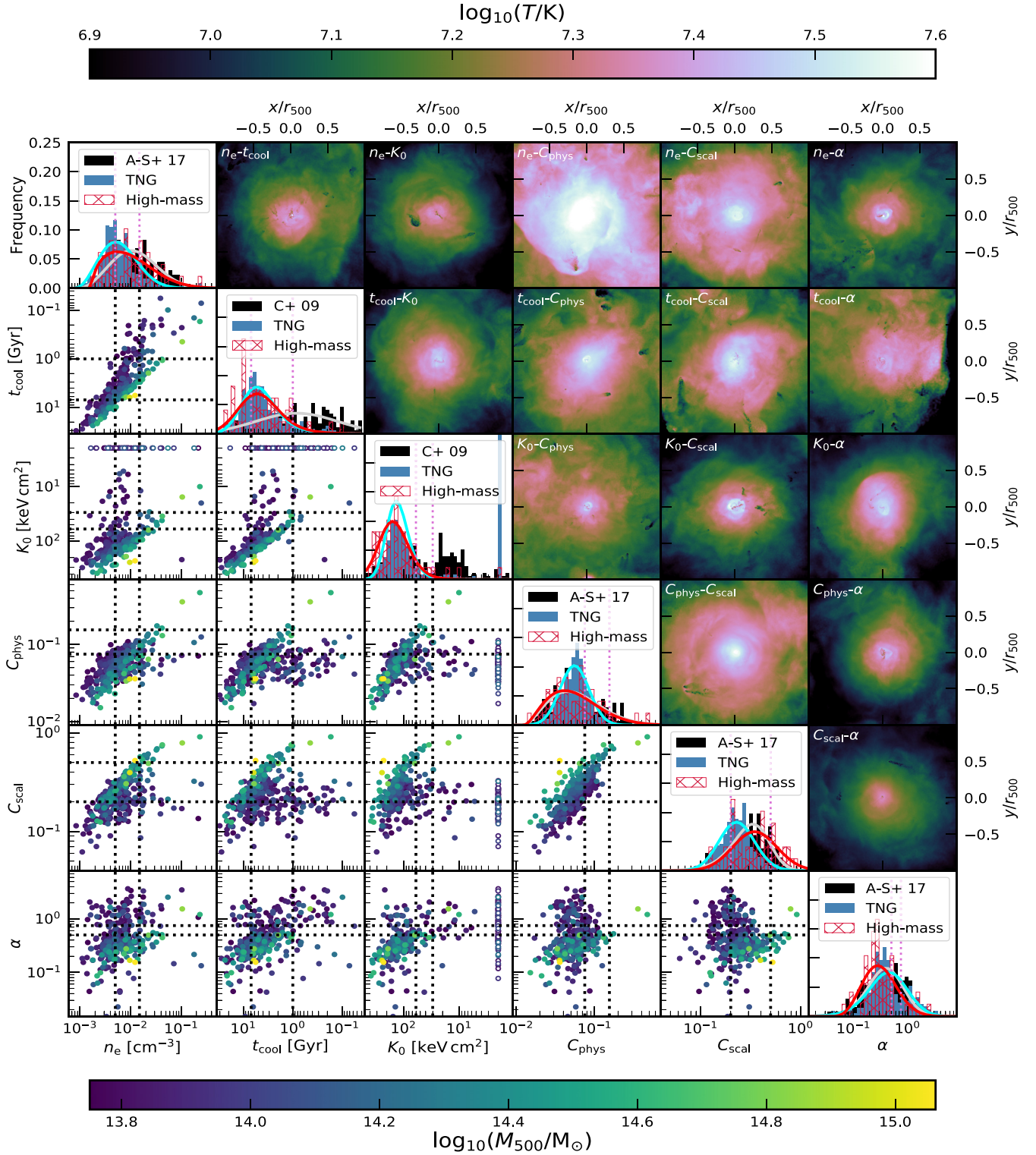


**Figure 4.** Comparison of the different CC criteria at  $z = 0$ . In the diagonal panels, we plot the complete sample (blue), the high-mass sample (red), and the observed sample (black) criteria distributions. We compare to the *Planck* ESZ sample (Andrade-Santos et al. 2017) [A-S+17] (for central electron number density, physical and scaled concentration parameter and cuspsiness parameter) and the *ACCEPT* sample (Cavagnolo et al. 2009) [C+09] (for cooling time and central entropy excess). The solid blue, red, and grey lines show the best-fitting lognormal distributions for the complete sample, the high-mass sample, and the observations, respectively. The lower off-diagonal panels show the simulated criteria correlations with colour denoting cluster mass, where we find increased scatter for low-mass systems, and the dashed lines denoting CC and MCC thresholds. In the upper off-diagonal panels we plot  $2r_{500} \times 2r_{500}$  mass-weighted temperature maps of randomly selected clusters that are defined as CC by both criteria.

**Table 3.** Correlation and scatter about the best-fitting power law for the different CC criteria at  $z = 0$ . The Spearman rank correlation coefficients,  $r_s$ , are shown in the lower off-diagonal entries and the scatter,  $\sigma_{\log_{10}}$ , in the upper off-diagonal entries. Errors are computed by bootstrap resampling 10 000 times.

Criterion	$n_e$	$t_{\text{cool}}$	$K_0$	$C_{\text{phys}}$	$C_{\text{scal}}$	$\alpha$
$n_e$	–	$0.19 \pm 0.01$	$0.35 \pm 0.03$	$0.31 \pm 0.02$	$0.36 \pm 0.03$	$0.38 \pm 0.03$
$t_{\text{cool}}$	$0.88 \pm 0.04$	–	$0.39 \pm 0.04$	$0.51 \pm 0.03$	$0.54 \pm 0.03$	$0.49 \pm 0.04$
$K_0$	$0.62 \pm 0.04$	$0.86 \pm 0.02$	–	$0.73 \pm 0.02$	$0.73 \pm 0.02$	$0.63 \pm 0.03$
$C_{\text{phys}}$	$0.58 \pm 0.04$	$0.49 \pm 0.05$	$0.41 \pm 0.05$	–	$0.12 \pm 0.01$	$0.18 \pm 0.01$
$C_{\text{scal}}$	$0.57 \pm 0.04$	$0.27 \pm 0.05$	$0.06 \pm 0.06$	$0.74 \pm 0.03$	–	$0.18 \pm 0.01$
$\alpha$	$0.31 \pm 0.06$	$0.52 \pm 0.05$	$0.62 \pm 0.04$	$0.20 \pm 0.05$	$-0.12 \pm 0.06$	–

distribution is poorest fit by a lognormal distribution with a large number of clusters yielding values just below the MCC threshold, which leads to lower than observed CC fraction. The observational sample has a mean value of 0.41 and a standard deviation of  $\sigma = 0.69$ .

In the upper off-diagonal panels of Fig. 4 we plot projected mass-weighted temperature maps of randomly selected simulated clusters that pass both CC criteria to demonstrate the range of systems that are classified as CCs. Each map is centred on the potential minimum of the cluster with a width of  $2r_{500} \times 2r_{500}$ , a depth of  $2r_{500}$ , and is projected along the  $z$ -axis. All maps show a central core, but there is significant variation in the surrounding structures.

#### 4.4 Criteria correlations

In the lower off-diagonal panels of Fig. 4, we plot the correlation of the different CC criteria for the complete sample, with the point colour denoting  $M_{500}$ . We note that for easier comparison we have inverted the  $t_{\text{cool}}$  and  $K_0$  axes, therefore CC clusters will always appear at the top or right side of a panel. In addition, we make those clusters with  $K_0 < 2 \text{ keV cm}^2$  visible on the plots by setting  $K_0 = 2 \text{ keV cm}^2$  for them. However, in quantifying the correlation coefficients of different CC criteria we use their fiducial values. We quantify the correlation between criteria using the Spearman rank correlation coefficient,  $r_s$ . In addition, we fit a simple power law of the form

$$\log_{10}(Y) = A + B \log_{10}(X/X_{\text{piv}}), \quad (8)$$

where  $A$  and  $B$  set the normalization and slope of the power law, respectively, and  $X_{\text{piv}}$  is the pivot point, which is set to the median value of the criterion  $X$ . This enables us to compute the scatter about the best fit via equation (7). The correlation coefficients and scatter values for the complete sample are summarized in Table 3, while the values for the high-mass sample are summarized in Appendix B.

First, we note that the correlation between criteria shows some mass dependence. Examining the  $n_e$ – $\alpha$  correlation for the complete sample yields a correlation coefficient of  $r_s = 0.31 \pm 0.06$ , with a scatter of  $\sigma_{\log_{10}} = 0.38 \pm 0.03$ . Selecting clusters with  $M_{500} > 2 \times 10^{14.0} M_{\odot}$  we find a significantly stronger correlation, with  $r_s = 0.75 \pm 0.10$  and a scatter of  $\sigma_{\log_{10}} = 0.33 \pm 0.04$ . This correlation coefficient is in better agreement with the observed value of  $r_s = 0.88$  found for the *Planck* ESZ sample (Andrade-Santos et al. 2017), which consists of clusters with  $M_{500} > 2 \times 10^{14} M_{\odot}$  due to the selection function.

The central electron number density criterion,  $n_e$ , is strongly correlated with  $t_{\text{cool}}$ ,  $C_{\text{phys}}$ , and  $C_{\text{scal}}$ , yielding correlation coefficients of  $0.88 \pm 0.04$ ,  $0.58 \pm 0.04$ , and  $0.57 \pm 0.04$ , respectively. These correlations are not unexpected as the cooling time depends on the central number density, see equation (1), and clusters with higher central densities should have higher central X-ray luminosities, due

to its  $n_e^2$  dependence. There is no obvious separation in the criteria space with cluster mass. The correlation of  $t_{\text{cool}}$  with the  $C_{\text{phys}}$  and  $C_{\text{scal}}$  criteria is significantly weakened by the increased scatter in these values for low-mass clusters, with correlation coefficients of  $0.49 \pm 0.05$  and  $0.27 \pm 0.05$  and scatter values of  $0.51 \pm 0.03$  and  $0.54 \pm 0.03$  for  $t_{\text{cool}}$ – $C_{\text{phys}}$  and  $t_{\text{cool}}$ – $C_{\text{scal}}$ , respectively. Lower mass clusters systematically scatter to shorter central cooling times for a given concentration parameter.

The central entropy excess,  $K_0$ , is strongly correlated with  $n_e$ ,  $t_{\text{cool}}$  and  $\alpha$ , producing correlation coefficients of  $0.62 \pm 0.04$ ,  $0.86 \pm 0.02$ , and  $0.62 \pm 0.04$ , respectively. There is a reasonable correlation with the concentration parameter measured within physical apertures with coefficient of  $0.41 \pm 0.5$ , but we find no correlation between  $K_0$  and  $C_{\text{scal}}$  with a coefficient value of  $-0.06 \pm 0.06$ . Low-mass clusters have increased scatter to smaller values of  $K_0$  for a given value of  $C_{\text{scal}}$  and many have a central entropy excess of zero, which results in no statistical correlation. We find a mild trend with mass for the  $K_0$ – $n_e$  and  $K_0$ – $C_{\text{scal}}$ , with  $n_e$  and  $C_{\text{scal}}$  values increasing with mass for a given  $K_0$  value.

We find a strong correlation between the physical and scaled concentration parameters, which is not that surprising. For the complete sample we find  $r_s = 0.74 \pm 0.03$  with a small level of scatter of  $\sigma_{\log_{10}} = 0.12 \pm 0.01$  about the best-fitting relation. We find a mass dependence for this correlation, with more massive clusters having a larger concentration parameter within physical apertures,  $C_{\text{phys}}$ , for a given concentration parameter within scaled apertures,  $C_{\text{scal}}$ . As noted above, this may be due to the distribution of gas with radius.

The cuspidity parameter,  $\alpha$ , is strongly correlated with  $t_{\text{cool}}$  ( $r_s = 0.63 \pm 0.04$ ) and  $K_0$  ( $0.60 \pm 0.04$ ), and weakly correlated with  $n_e$  ( $r_s = 0.33 \pm 0.06$ ) and  $C_{\text{phys}}$  ( $r_s = 0.23 \pm 0.06$ ). However, it has some of the largest levels of scatter, with  $t_{\text{cool}}$  and  $K_0$  producing values of  $0.52 \pm 0.05$  and  $0.62 \pm 0.04$ , respectively.

In summary, we find that the correlation between different CC criteria is mass dependent, with an increasing correlation between criteria for more massive clusters. Low-mass clusters appear to scatter to lower central entropy excess values. Although correlated with other criteria the cuspidity parameter has some of the largest levels of scatter. The two quantities that are most correlated are the central electron number density and the central cooling time.

## 5 EVOLUTION WITH REDSHIFT

### 5.1 CC fraction evolution

Having examined the CC fraction at  $z = 0$  for the different criteria, we now compare the evolution of the CC fraction with redshift. The success of large SZ surveys with dedicated follow-up has resulted in a large number of clusters being detected out to  $z \approx 2$ , due to the redshift independence of the SZ effect. This provides a large

sample of clusters that is free from CC bias (Lin et al. 2015) and enables a fair comparison of the redshift evolution of the simulated and observed CC fractions. We use the *Planck* ESZ and *ACCEPT* samples as a low-redshift ( $z < 0.25$ ) bin, with the latter's CC fractions corrected for the expected CC bias. The *SPT-XVP* sample is then divided into three bins over the redshift range  $0.25 < z < 1.2$ , with CC criteria values taken from McDonald et al. (2013). For the central electron number density we additionally include the *SPT-Hiz* sample to form a high-redshift bin ( $1.2 < z < 1.9$ ). The *Planck* ESZ and *ACCEPT* samples are both centred on the X-ray peak and for consistency we select the X-ray peak centred CC fractions for the SPT samples. McDonald et al. (2013) investigated the impact of centring choice and found no impact on the number of strong CCs found. In addition, for relaxed clusters the densest and strongest X-ray emitting gas will reside at the potential minimum and the centre of the simulated clusters is chosen to be the potential minimum. We note that the redshifts of SPT clusters (Bleem et al. 2015) have been updated since McDonald et al. (2013) and this results in slightly different CC fractions compared to the original paper. The  $1\sigma$  confidence intervals on both the observed and simulated samples are calculated via the beta distribution quantile technique (Cameron 2011), due to low number statistics at high redshift. We note that McDonald et al. (2013) find similar low-redshift CC fractions to other low-redshift observations when analysing the Vikhlinin et al. (2009a) cluster sample with the SPT pipeline, indicating that the systematic impact of using different observational samples at low redshift is likely small.

The complete sample has a lower median mass than the observational samples, due to observational selection functions and the limited volume of the simulation. Therefore, for each criterion we compare how the observed CC fraction evolves with redshift to both the complete and high-mass samples. At  $z = 1$ , the mass bins contain 45, 30, and 2 clusters and have median  $M_{500}$  values of  $6.8 \times 10^{13}$ ,  $1.1 \times 10^{14}$ , and  $2.8 \times 10^{14} M_{\odot}$ , respectively. We summarize the fraction of clusters defined as CC, MCC, and NCC at  $z = 1$  in Table 4. Additionally, we also examine the evolution only over the redshift range of the *SPT-XVP* sample ( $0.25 < z < 1.2$ ) to ensure that differing low-redshift samples and low number statistics at  $z > 1.2$  do not impact the result. We do not examine the evolution of the concentration parameter with scaled apertures as there are no high-redshift ( $z > 0.25$ ) observational constraints. To enable a quantitative comparison, we fit both the observed and simulated CC fraction as a function of redshift with a linear relation ( $y = mx + c$ ) using the Levenberg–Marquardt algorithm and accounting for the uncertainty in the CC fractions.

In Fig. 5, we plot the CC fraction, defined by the central electron number density, for the complete sample (left-hand panel) and the high-mass sample (right-hand panel). As noted in the previous section the high-mass sample leads to higher normalization at low redshift and the high-mass sample has a consistently greater CC fraction at fixed redshift. The CC fractions of the high-mass sample are in agreement with the observed, however the uncertainty is large due to the small sample size. To quantify the redshift evolution we fit a linear relation to the CC fraction as a function of redshift. With best-fitting slopes of  $0.64 \pm 0.05$  and  $0.55 \pm 0.10$ , respectively, the complete and high-mass samples have a consistent redshift evolution. This is significantly steeper than the observed evolution, which has a slope of  $0.24 \pm 0.08$ . If we only compare to the *SPT-XVP* sample ( $0.25 < z < 1.2$ ), we find that the simulated slope steepens further for the complete sample. The observed CC fraction slowly decreases from  $z = 2$  to  $z = 0$ . In contrast, the reduction in the CC fraction for the simulated samples begins later and

results in a much more rapid decline. The high-mass sample begins to decline at lower redshift than the complete and then proceeds at the same rate, leading to a higher normalization.

We examine the evolution of the CC fraction defined by the central cooling time criterion with redshift in Fig. 6. Though noisy and somewhat uncertain, there is tentative agreement between the high-mass CC fractions and the observations for  $z > 0.25$ . At lower redshift, the simulations have lower CC fractions. Fitting for the redshift evolution, we find that the complete sample produces a steeper slope of  $0.60 \pm 0.05$  compared to the high-mass sample slope of  $0.37 \pm 0.09$ . The high-mass sample slope is  $2\sigma$  steeper than the observed slope of  $0.17 \pm 0.10$ . If the considered redshift range is narrowed to  $0.25 < z < 1.2$  the complete and high-mass samples yield consistent slopes that are steeper than observed.

Defining CCs via the central entropy excess yields very similar results to the central cooling time, as shown in Fig. 7. The high-mass sample produces CC fractions in reasonable agreement with the observed CC fractions, and a lower normalization relative to the complete sample. The discrepancy at low-redshift between the high-mass sample and the observed sample may be larger as the low-redshift observed CC fraction is likely a lower limit due to the limited resolution of the temperature profiles. Fitting the CC fractions we find the slope of the complete sample,  $0.55 \pm 0.05$ , is steeper than the slope of the high-mass sample,  $0.32 \pm 0.09$ . The high-mass sample slope is  $>2\sigma$  steeper than the observed slope of  $0.08 \pm 0.06$ . When the redshift range is restricted, the complete sample and the high-mass sample produce slopes that are consistent, but steeper than observed. We note that the limited observational resolution and a potentially higher low-redshift CC fraction would further flatten the observed redshift evolution of the CC fraction.

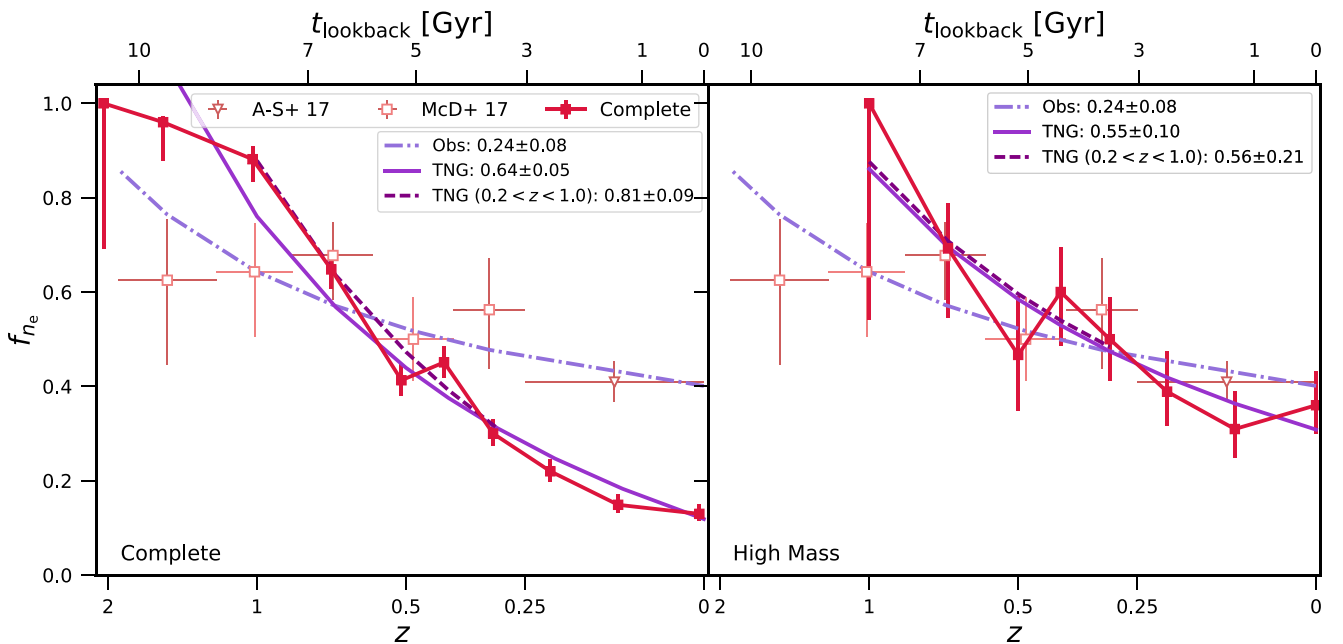
In Fig. 8, we plot the observed and simulated CC fraction evolution with redshift for clusters defined as CCs by the concentration parameter within physical apertures. It is clear that the complete sample does not evolve linearly with redshift, producing a more rapid increase in CC fraction with increasing redshift. The linear fit to the complete sample CC fractions is therefore poor, but it yields a best-fitting slope of  $0.03 \pm 0.02$ . The high-mass sample yields a slope of  $-0.12 \pm 0.03$  that is in reasonable agreement with the observed slope of  $-0.07 \pm 0.07$ . However, the normalization of the simulated sample is consistently lower than the observed CC fraction at all redshifts by  $\sim 0.15$ . Restricting the redshift range over which the linear relation is fit leads to negligible change in the slopes produced by the simulated samples.

Classifying clusters by the cuspsness parameter, as shown in Fig. 9, we find that the complete sample yields a roughly linear redshift evolution, but the CC fraction decreases for the highest redshift bin. The complete sample yields a slope of  $0.28 \pm 0.06$ . The CC fraction of the high-mass sample is very noisy, with a lower CC fraction at low redshift compared to the complete sample that generally increases with redshift. The best-fitting slope of the high-mass sample is  $0.03 \pm 0.16$ , but is a comparatively poorer fit compared to the complete sample. The observed sample produces a slope of  $-0.14 \pm 0.04$ . If the redshift range of the comparison is restricted then both simulated samples produce a positive slope with increasing redshift, but the trend for the high-mass sample is very uncertain and still consistent with no redshift evolution.

If the entire cluster volume evolves in a self-similar manner the properties of the core should change with redshift and this would result in the evolution of the CC fraction with redshift. Clusters are defined as overdensities relative to the critical density of the Universe, which increases with increasing redshift. This results in clusters of a fixed mass increasing in density with increasing red-

**Table 4.** Table of the fraction of clusters defined as CC, MCC, or NCC at  $z = 1$  for the criteria presented in Section 3 for the complete sample and the different mass bins. The  $1\sigma$  uncertainties are computed by the beta distribution quantile technique.

Sample ( $z = 1$ )	Fraction	Criteria					
		$n_e$	$t_{\text{cool}}$	$K_0$	$C_{\text{phys}}$	$C_{\text{scal}}$	$\alpha$
Complete ( $M_{500} > 10^{13.75} M_{\odot}$ ) $N = 77$	CC	$0.87^{+0.03}_{-0.05}$	$0.81^{+0.04}_{-0.05}$	$0.83^{+0.03}_{-0.05}$	$0.08^{+0.04}_{-0.02}$	$0.00^{+0.02}_{-0.00}$	$0.48^{+0.06}_{-0.06}$
	MCC	$0.10^{+0.05}_{-0.03}$	$0.18^{+0.05}_{-0.04}$	$0.09^{+0.04}_{-0.02}$	$0.45^{+0.06}_{-0.05}$	$0.43^{+0.06}_{-0.05}$	$0.16^{+0.05}_{-0.03}$
	NCC	$0.01^{+0.03}_{-0.00}$	$0.00^{+0.02}_{-0.00}$	$0.08^{+0.04}_{-0.02}$	$0.47^{+0.06}_{-0.06}$	$0.57^{+0.05}_{-0.06}$	$0.36^{+0.06}_{-0.05}$
Low-mass ( $M_{500} < 9.0 \times 10^{13} M_{\odot}$ ) $N = 45$	CC	$0.87^{+0.04}_{-0.07}$	$0.87^{+0.04}_{-0.07}$	$0.93^{+0.02}_{-0.06}$	$0.11^{+0.06}_{-0.03}$	$0.00^{+0.04}_{-0.00}$	$0.56^{+0.07}_{-0.07}$
	MCC	$0.09^{+0.06}_{-0.03}$	$0.11^{+0.06}_{-0.03}$	$0.02^{+0.05}_{-0.01}$	$0.44^{+0.07}_{-0.07}$	$0.33^{+0.08}_{-0.06}$	$0.13^{+0.07}_{-0.04}$
	NCC	$0.02^{+0.05}_{-0.01}$	$0.00^{+0.04}_{-0.00}$	$0.04^{+0.07}_{-0.01}$	$0.44^{+0.07}_{-0.07}$	$0.67^{+0.06}_{-0.08}$	$0.31^{+0.08}_{-0.06}$
Intermediate-mass ( $9.0 \times 10^{13} \leq M_{500} < 2.0 \times 10^{14} M_{\odot}$ ) $N = 30$	CC	$0.87^{+0.04}_{-0.09}$	$0.73^{+0.06}_{-0.09}$	$0.70^{+0.07}_{-0.09}$	$0.03^{+0.07}_{-0.01}$	$0.00^{+0.06}_{-0.00}$	$0.37^{+0.09}_{-0.08}$
	MCC	$0.13^{+0.09}_{-0.04}$	$0.27^{+0.09}_{-0.06}$	$0.17^{+0.09}_{-0.05}$	$0.50^{+0.09}_{-0.09}$	$0.53^{+0.09}_{-0.09}$	$0.20^{+0.09}_{-0.05}$
	NCC	$0.00^{+0.05}_{-0.00}$	$0.00^{+0.04}_{-0.00}$	$0.13^{+0.05}_{-0.04}$	$0.47^{+0.07}_{-0.09}$	$0.47^{+0.06}_{-0.09}$	$0.43^{+0.08}_{-0.08}$
High-mass ( $M_{500} \geq 2.0 \times 10^{14} M_{\odot}$ ) $N = 2$	CC	$1.00^{+0.00}_{-0.46}$	$0.50^{+0.25}_{-0.25}$	$0.50^{+0.25}_{-0.25}$	$0.00^{+0.46}_{-0.00}$	$0.00^{+0.46}_{-0.00}$	$0.50^{+0.25}_{-0.25}$
	MCC	$0.00^{+0.46}_{-0.00}$	$0.50^{+0.25}_{-0.25}$	$0.50^{+0.25}_{-0.25}$	$0.00^{+0.46}_{-0.00}$	$1.00^{+0.00}_{-0.46}$	$0.00^{+0.46}_{-0.00}$
	NCC	$0.00^{+0.46}_{-0.00}$	$0.00^{+0.46}_{-0.00}$	$0.00^{+0.46}_{-0.00}$	$1.00^{+0.00}_{-0.46}$	$0.00^{+0.46}_{-0.00}$	$0.50^{+0.25}_{-0.25}$

**Figure 5.** Evolution of the CC fraction, defined central electron number density, with redshift for the complete (left-hand panel) and high-mass (right-hand panel) samples (solid red line). We compare to the observed evolution for the same CC criterion from the combination of Andrade-Santos et al. (2017, open circle) and McDonald et al. (2017, open squares). The dash-dotted, solid, and dashed purple lines show the best-fitting linear redshift evolution for the observed sample, the simulated sample, and the simulated sample in the redshift range  $0.2 < z \leq 1.0$ , respectively, with the slopes given in the legend. The simulated evolution is consistent between the two different samples, but both samples are steeper than the observed evolution. Limiting the redshift range of the simulated samples results in a further steepening of the evolution.

shift. Measuring the electron number density at fixed fraction of a radius relative to this overdensity will result in it being measured closer to the cluster centre with increasing redshift and it will increase. This results in a greater fraction of clusters being defined as CC for a fixed physical threshold. From equation (1), it is clear that an increasing number density will result in a decreasing cooling time and for a fixed threshold the fraction of clusters defined as CC via their central cooling time should increase with redshift. The concentration parameter within physical apertures should yield a greater CC fraction with redshift because the inner aperture will include an increasing fraction of the X-ray emission and the outer aperture will remain roughly unchanged due to the  $n_e^2$  dependence of the emission. The properties of cluster cores are observed to remain relatively unchanged with redshift (McDonald et al. 2017), while the rest of the cluster volume follows the expected

self-similar expectation. Therefore, differences in the observed and simulated slope, i.e. the redshift evolution, may be driven by differences in how the thermodynamic properties of the core change with redshift.

## 5.2 Relaxed fraction

CC clusters are often associated with more spherical and regular X-ray morphologies. Previous numerical work has shown that close to head-on major mergers can disrupt a CC (Rasia et al. 2015; Hahn et al. 2017), which suggests that a greater fraction of NCC clusters should be disturbed at low redshift. Additionally, radio haloes that are associated with recent merger activity have, to date, only been observed in NCC clusters, which suggests that a greater fraction of

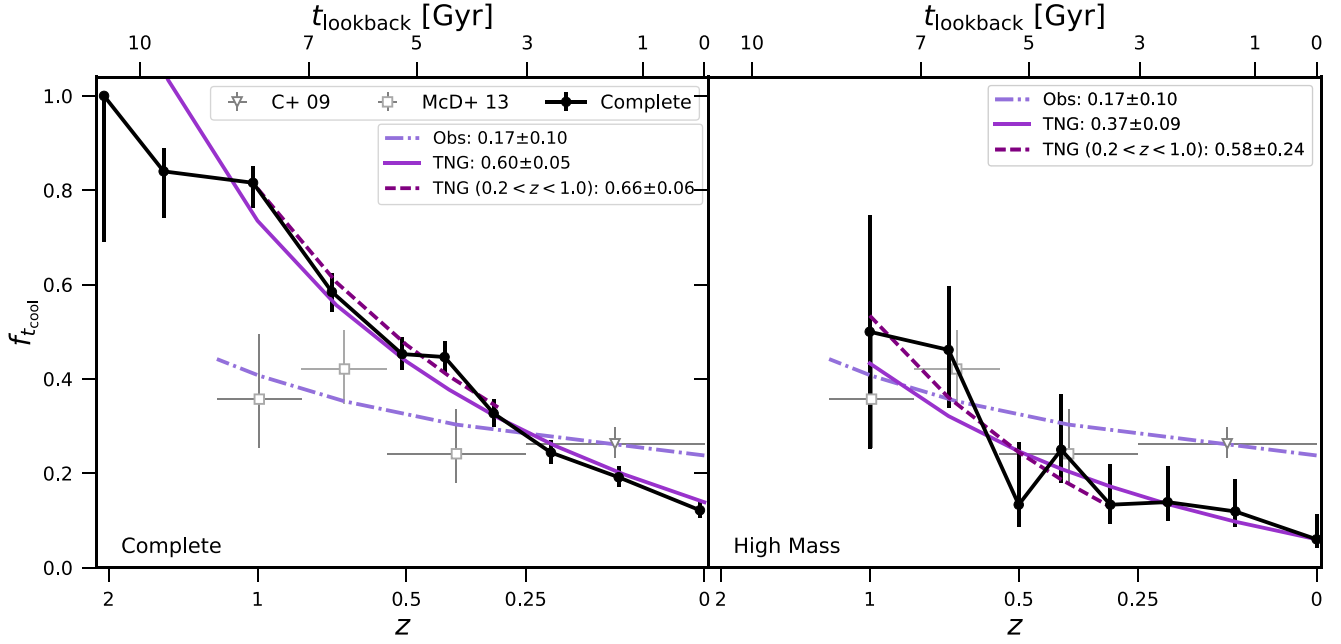


**Figure 6.** Evolution of the CC fraction with redshift for the complete (left-hand panel) and high-mass (right-hand panel) samples (solid black line), defined by the central cooling time criterion. We compare to the observed evolution from the combination of bias corrected Cavagnolo et al. (2009, open circle) and McDonald et al. (2013, open squares). The fit line styles are the same as in Fig. 5. The evolution with redshift for both simulated samples is steeper than the observed evolution.

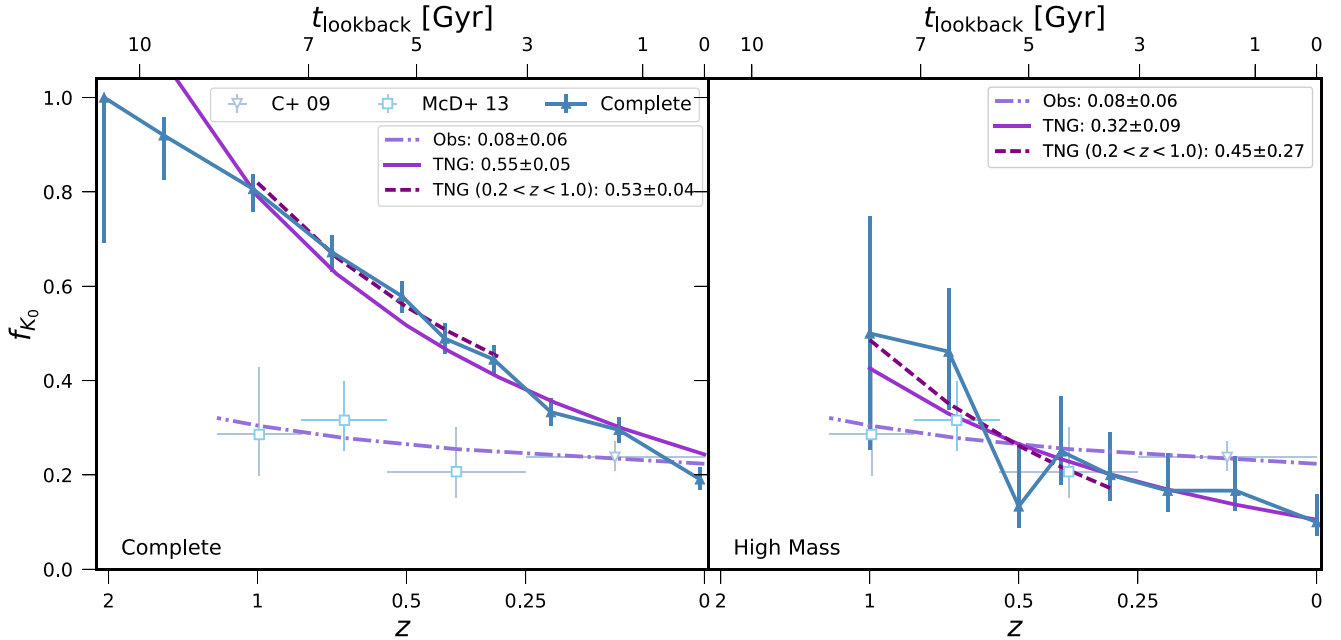


**Figure 7.** Evolution of the CC fraction with redshift for the complete (left-hand panel) and high-mass (right-hand panel) samples (solid blue line), defined by the central entropy excess criterion. We compare to the observed evolution from the combination of bias corrected Cavagnolo et al. (2009, open circle) and McDonald et al. (2013, open squares). The fit line styles are the same as in Fig. 5. The evolution with redshift for both simulated samples is steeper than the observed evolution.

NCC clusters should have undergone recent mergers (Cassano et al. 2010). We now examine the fraction of clusters that are defined as relaxed and the fraction of CC and NCC clusters that are defined as relaxed as a function of redshift. Theoretically, there are many ways of defining a relaxed cluster (Neto et al. 2007; Duffy et al. 2008; Klypin, Trujillo-Gomez & Primack 2011; Dutton & Macciò 2014; Klypin et al. 2016). We follow Barnes et al. (2017b) and define a

cluster as relaxed if

$$E_{\text{kin},500}/E_{\text{therm},500} < 0.1, \quad (9)$$

where  $E_{\text{kin},500}$  is the sum of the kinetic energy of the gas cells, with the bulk motion of the cluster removed, inside  $r_{500}$ . This should account for any motions generated by substructures or the centre of mass being offset from the potential minimum.  $E_{\text{therm},500}$  is the

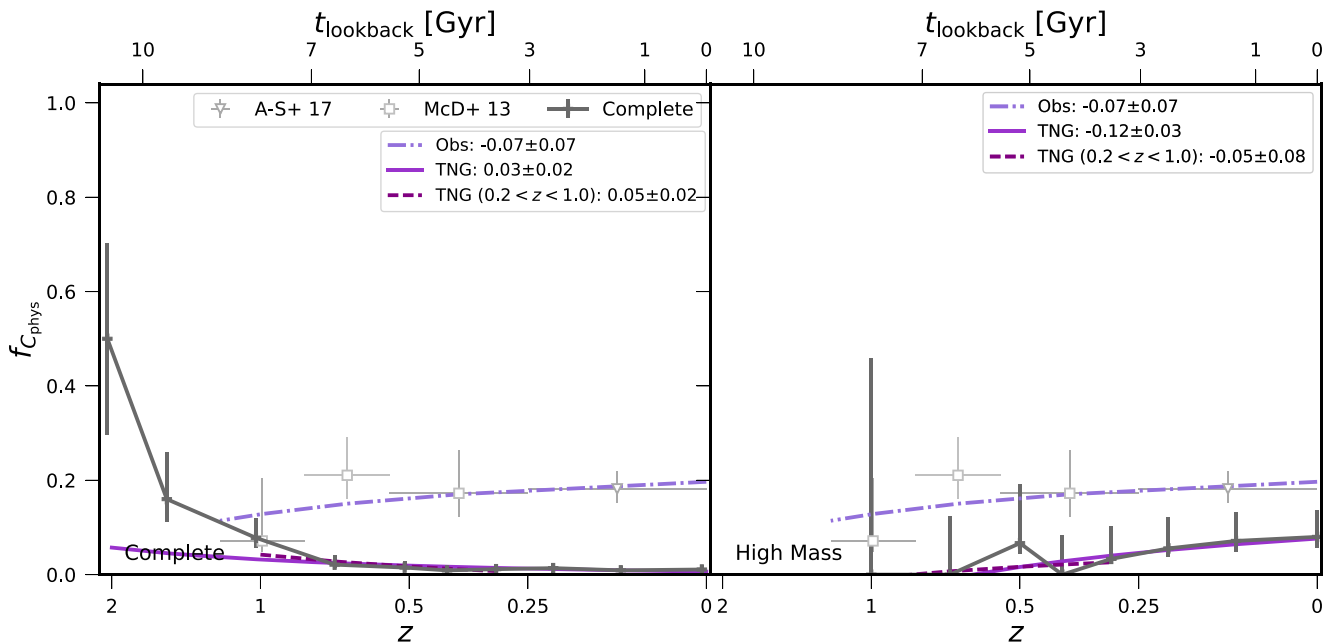


**Figure 8.** Evolution of the CC fraction with redshift for the complete (left-hand panel) and high-mass (right-hand panel) samples (solid grey line), defined by the concentration parameter within physical apertures. We compare to the observed evolution from the combination of Andrade-Santos et al. (2017, open circle) and McDonald et al. (2013, open squares). The fit line styles are the same as in Fig. 5. Selecting high-mass clusters results in a flatter and positive evolution with redshift that is more consistent with the observed evolution, however the normalization of the CC fraction is 0.15 lower than observed.

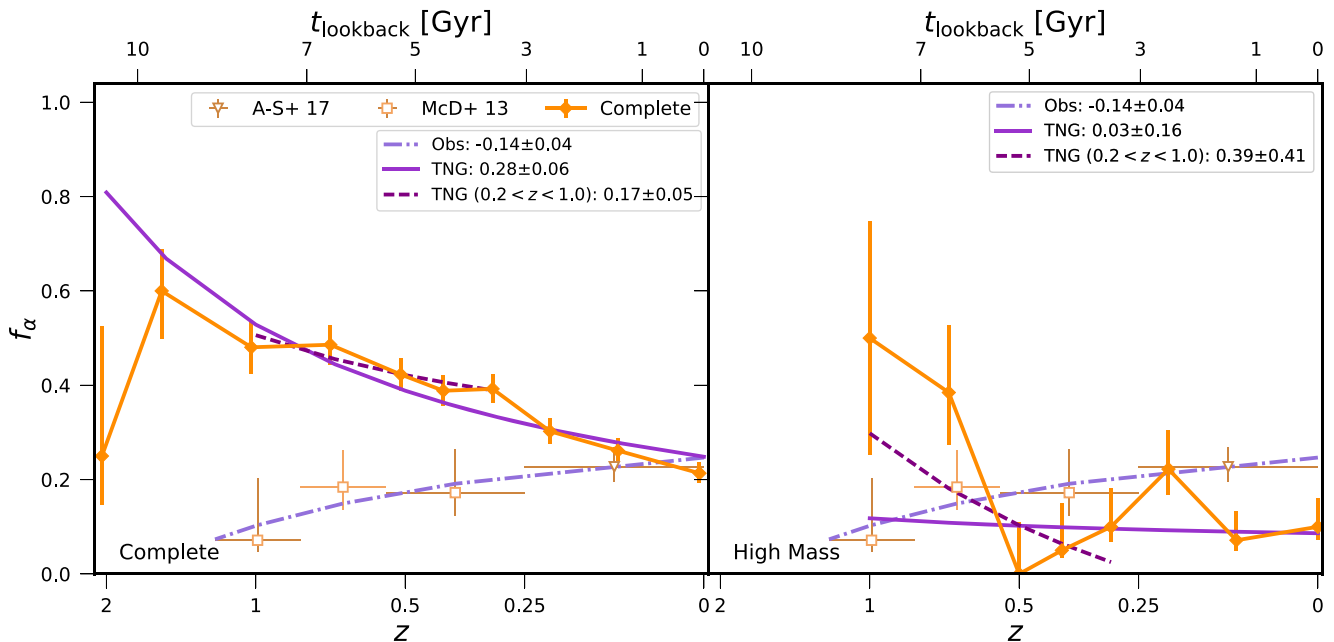


**Figure 9.** Evolution of the CC fraction with redshift for the complete (left-hand panel) and high-mass (right-hand panel) samples (solid yellow line), defined by the cuspsiness parameter. We compare to the observed evolution from the combination of Andrade-Santos et al. (2017, open circle) and McDonald et al. (2013, open squares). The evolution with redshift for both simulated samples is consistent, however the evolution of the observed sample has a positive slope towards low redshift and the simulated evolution is negative.

sum of the thermal energy of the gas cells within  $r_{500}$ . As clusters relax they will thermalize, converting kinetic energy to thermal energy via weak shocks (e.g. Kunz et al. 2011) and potentially turbulent cascades (Zhuravleva et al. 2014). We demonstrate in Appendix C that using other metrics to define a relaxed cluster, such as substructure fraction or centre of mass offset, yield similar

results. We note that the selected threshold for the ratio of kinetic to thermal energy is designed to yield a relaxed sample, as opposed to other criteria that select thresholds to remove the most disturbed objects.

In Fig. 10, we plot the relaxed fraction as a function of redshift in both panels, where we have split the criteria for clarity. The fraction

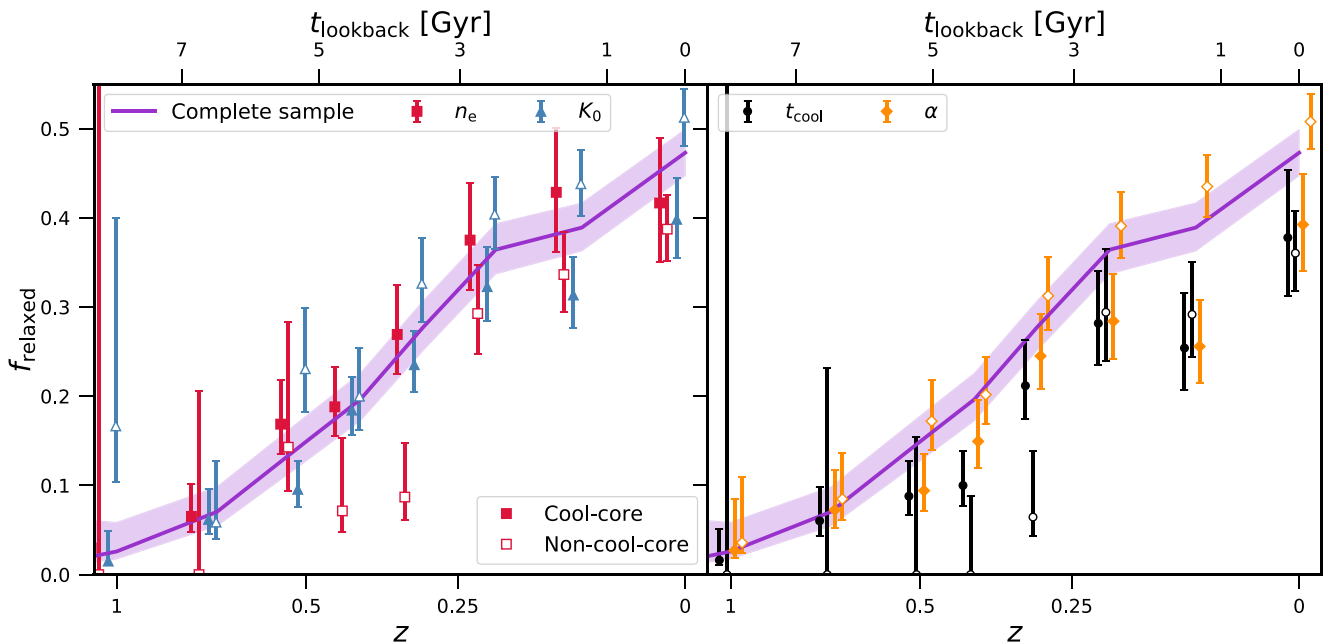


**Figure 10.** Fraction of clusters defined as relaxed as a function of redshift. We plot the relaxed fraction for the complete sample (purple line), those complete sample clusters defined as CCs (filled symbols) and those complete sample clusters defined as NCC (open symbols). CCs are defined via the central electron number density (red square), cooling time (black circle), central entropy excess (blue triangle) and the cuspsiness parameter (yellow diamond) criteria. The shaded region and error bars denote  $1\sigma$  confidence intervals, calculated via the beta distribution quantile technique. The CC and NCC points are divided between the two panels and marginally offset for clarity. We find no conclusive evidence that a greater fraction of CCs, defined by any criteria, are defined as relaxed compared to the NCC or complete samples.

of the complete sample defined as relaxed decreases with increasing redshift, from  $45 \pm 3$  per cent at  $z = 0$  to  $3 \pm 1$  per cent at  $z = 1$ . The increased kinetic energy of the cluster gas with increasing redshift has been shown in previous numerical work (Stanek et al. 2010; Barnes et al. 2017a; Le Brun et al. 2017), which is consistent with the picture that the merger rate at higher redshift is larger (McBride, Fakhouri & Ma 2009; Fakhouri, Ma & Boylan-Kolchin 2010; Giocoli, Tormen & Sheth 2012) and that clusters have had less time to thermalize at high redshift. This picture is consistent with observational results if the crossing time of clusters decreases with increasing redshift (Mantz et al. 2015; McDonald et al. 2017; Nurgaliev et al. 2017), which it does if we assume self-similar evolution (Carlberg et al. 1997).

In addition, we plot the fraction of complete sample that is defined as CCs or NCCs that are classified as relaxed, via the central electron number density and the central entropy excess in the left-hand panel, and the central cooling time and cuspsiness parameter in the right-hand panel. We do not show the concentration parameter because it is noisy as it only defines a small number of clusters as CC. We are limited to  $z \leq 1$  due to small number statistics at high redshift. Defining CCs and NCCs by the central electron number density, we find that the fraction of relaxed clusters in both samples is broadly consistent with the complete sample, decreasing from  $42 \pm 7$  per cent and  $39 \pm 4$  per cent at  $z = 0$  to  $13 \pm 5$  per cent and  $14_{-5}^{+14}$  per cent at  $z = 0.5$  for the CC and NCC samples, respectively. For  $z > 0.5$  no clusters are defined as NCC. We find that the fraction of CCs defined as relaxed is consistent within  $2\sigma$  of the fraction of NCCs defined as relaxed at all redshifts. Defining clusters as CC or NCC by their central entropy excess, there is some evidence that the fraction of NCC clusters defined as relaxed is greater than the fraction of CC clusters defined as relaxed, but the fractions are consistent within  $2\sigma$ . We find that  $37 \pm 6$  per cent and  $49 \pm 3$  per

cent at  $z = 0$  and  $10 \pm 3$  and  $23 \pm 5$  per cent at  $z = 0.5$  of clusters are defined as relaxed for the CC and NCC samples, but we note that many CCs have a central entropy excess of zero. For  $z > 0.5$  no clusters are defined as NCC.

Using central cooling time as the defining criteria, we find that the fraction of the CC sample defined as relaxed is consistent with the relaxed fractions for the NCC and the complete samples. At  $z = 0$ ,  $38 \pm 7$  per cent of CC clusters are defined as relaxed, compared to  $36 \pm 5$  per cent for the NCC sample. In contrast, defining CCs via the cuspsiness parameter we find that at low redshift ( $z < 0.25$ ) the fraction of CC clusters defined as relaxed is lower than for the NCC sample. We find that  $41 \pm 5$  per cent and  $50 \pm 3$  per cent of CCs and NCCs, respectively, are defined as relaxed at  $z = 0$ . At higher redshifts, the fraction of CCs and NCCs defined as relaxed are consistent with each other and the relaxed fraction of the complete sample. Overall, we find little evidence that the simulated CC samples have a higher relaxed fraction compared to either the NCC sample or the complete sample for any of the CC criteria that we have examined. We stress that this result holds for other theoretical methods of defining a relaxed cluster, such as substructure fraction and centre of mass offset. For the central entropy excess and the cuspsiness parameter criteria, the fraction of NCC clusters defined as relaxed is larger than fraction of CC clusters defined as relaxed. However, the difference is marginal and we would require a significantly larger sample to investigate this further.

In summary, we find that the simulated CC fraction evolves significantly more with redshift than the observed fraction. The process that converts CCs to NCCs appears to begin later in the simulations but acts much more rapidly. We find no evidence that the relaxed fraction of CCs is greater than NCCs or the complete cluster sample, suggesting that mergers are not solely responsible for disrupting

CCs. We stress that, as shown in Appendix C, these results hold for other theoretical methods of defining a relaxed cluster.

## 6 CORE EVOLUTION

We now examine how the properties of the average simulated cluster core evolves for CC, MCC, and NCC clusters. McDonald et al. (2017) demonstrated that the cores of CC clusters present in the SPT samples have evolved little since  $z \geq 1.5$ , with the rest of the cluster volume evolving in a manner consistent with the self-similar expectation. All profiles are computed in the range  $10^{-3} - 1.5 r_{500}$  using 50 radial bins. Only non-star-forming gas that is cooling, i.e. not being heated via supernovae or AGN feedback, with a temperature  $T > 1.0 \times 10^6$  K is included in the profiles. We use the central electron number density, central cooling time, and cuspsiness parameter as CC criteria in this section. Both concentration parameters yield very few CCs at  $z = 0$ , which makes the median profiles too noisy, while the central entropy excess yields a large number of clusters with a negligible central entropy which may be the result of missing physical processes. Where appropriate we normalize by the profiles at  $z = 0$  by the expected virial quantity of the cluster. These quantities are defined as

$$k_B T_{500} = \frac{GM_{500}\mu m_p}{2r_{500}}, \quad (10)$$

$$P_{500} = 500 f_b k_B T_{500} \frac{\rho_{\text{crit}}}{\mu m_p}, \quad (11)$$

$$K_{500} = \frac{k_B T_{500}}{(500 f_b \rho_{\text{crit}} / \mu_e m_p)^{2/3}}, \quad (12)$$

where  $k_B$  is the Boltzmann constant,  $G$  is the gravitational constant,  $\mu = 0.59$  is the mean molecular weight,  $m_p$  is the proton mass,  $\rho_{\text{crit}} \equiv E^2(z)(3H_0^2/8\pi G)$ ,  $H_0$  is the Hubble constant and  $E(z) \equiv (\Omega_M(1+z)^3 + \Omega_\Lambda)^{1/2}$ .

### 6.1 Electron number density profiles

In Fig. 11, we plot the median electron number density profiles at  $z = 0$  in the top row of panels. We divide the clusters into CC, MCC, and NCC samples via the central electron number density, central cooling time, and cuspsiness parameter in the left-hand, centre, and right-hand panels, respectively. The shaded/hatched region denotes the region that encompasses 68 per cent of the sample. The median CC, MCC, and NCC profiles defined by the central electron number density criterion are in good agreement for  $r > 0.1 r_{500}$ , but the CC profile diverges inside of this radius. The median CC central density is a factor  $\approx 2.5$  greater than the median MCC profile, which in turn is 30 per cent higher than the median NCC profile. Dividing clusters by their central cooling time the profiles begin to diverge at  $r = 0.1 r_{500}$ , reach a central density that is a factor 2 lower than central electron number density criterion, and have a significantly larger spread. When the sample is classified by the cuspsiness parameter we find that the CC, MCC, and NCC median profiles are all consistent with each other within the  $1\sigma$  uncertainties at all radii.

In the bottom row of panels, we plot the ratio of the median CC, MCC, and NCC profiles at  $z = 0$  over the median CC, MCC, and NCC profiles at  $z = 1$ . Note the samples are redefined at  $z = 1$  and clusters can change from a CC to NCC, vice versa, or disappear from the sample between the two redshifts, for example by dropping below the mass threshold of  $M_{500} > 10^{13.75} M_\odot$  at high redshift. If the profile has not evolved we would expect the ratio

to be unity, i.e.  $n_e^{z=0}(r/r_{500}) = n_e^{z=1}(r/r_{500})$ . The self-similar model (Kaiser 1986) is scale free and so all overdensities will evolve in the same manner and the ratio would produce a value of  $1/E^2(z = 1) = 0.316$ . The uncertainty in the ratio is calculated by bootstrap resampling the  $z = 0$  and  $z = 1$  samples 10 000 times. All profiles evolve in reasonable agreement with the self-similar expectation for  $r > 0.1 r_{500}$ . Inside this radius the CC ratio diverges from the NCC ratio when separating clusters by their central electron number density. The CC ratio begins to rise at  $r = 0.1 r_{500}$  and reaches a peak value of 0.60, while the MCC ratio begin rising at  $r = 0.03 r_{500}$  and reaches a peak value of 0.60. The NCC ratio reaches a peak value of 0.42. In contrast, using the central cooling time or the cuspsiness parameter as the CC criterion results in all ratios being consistent with expected self-similar evolution at all radii, except at  $0.01 r/r_{500}$  where the ratio is less than the self-similar expectation for the cuspsiness parameter. We conclude that the extent to which the density of the typical cluster core has evolved is dependent on the CC criteria used. For the central electron number density the profiles have evolved more than observed since  $z = 1$  (McDonald et al. 2017), but less than the self-similar expectation.

### 6.2 Temperature profiles

We plot the median CC, MCC, and NCC temperature profiles at  $z = 0$  in the top row of Fig. 12. For  $r > 0.1 r_{500}$  the median CC, MCC, and NCC profiles are consistent with each other, within the scatter, for all CC criteria. Inside this radius, the central cooling time criterion produces a CC profile that reduces to a third of the peak value, while the MCC and NCC profiles are flat to the centre. Classifying clusters by the cuspsiness parameter produce a central CC profile that reduces by a third, an MCC profile that shows a modest reduction and a flat NCC profile. The central electron number density criterion produces a CC profile that shows a mild reduction in the central temperature, with the MCC and NCC profiles flattening in the core. The CC profile shows significantly more scatter compared to other criteria. The increased scatter in the CC profile is due to the fact that the criteria has a consistent number of clusters in each mass bin, which results in a greater spread in the normalization of the temperature profile as more massive clusters are hotter due to their deeper potential wells. The other criteria preferentially select haloes from one mass bin, which makes the normalization of their temperature profiles more consistent. All profiles begin to rise again at  $\sim 0.005 r_{500}$ , which may be a sign of ongoing AGN activity.

The bottom panels show the ratio of median temperature profiles at  $z = 0$  and  $z = 1$ . If the profile has evolved self-similarly this ratio would be  $1/E^{2/3}(z = 1) = 0.681$ . For  $r \geq 0.1 r_{500}$  all profiles are consistent with the expected self-similar evolution. The exception is the central electron number density CC profile which has cooled less than expected, but we note this profile has a very large scatter at  $z = 0$ . Inside this radius the ratios defined by the central electron number density and cuspsiness parameter criteria rise to values consistent with or greater than no evolution, suggesting the cores have gotten hotter since  $z = 1$ . In contrast, if the clusters are classified by the central cooling time or cuspsiness parameter then the cores evolve in line with the self-similar expectation, which they have cooled since  $z = 1$ . McDonald et al. (2014) found that the temperature in the cluster core has increased relative to the characteristic cluster temperature,  $T_{500}$ , towards lower redshift. However, these clusters were split by the cuspsiness parameter, with the ‘cuspiest’ 50 per cent of clusters defined as CC. It is not clear how this division, rather than by a fixed threshold, changes the observed evolution.

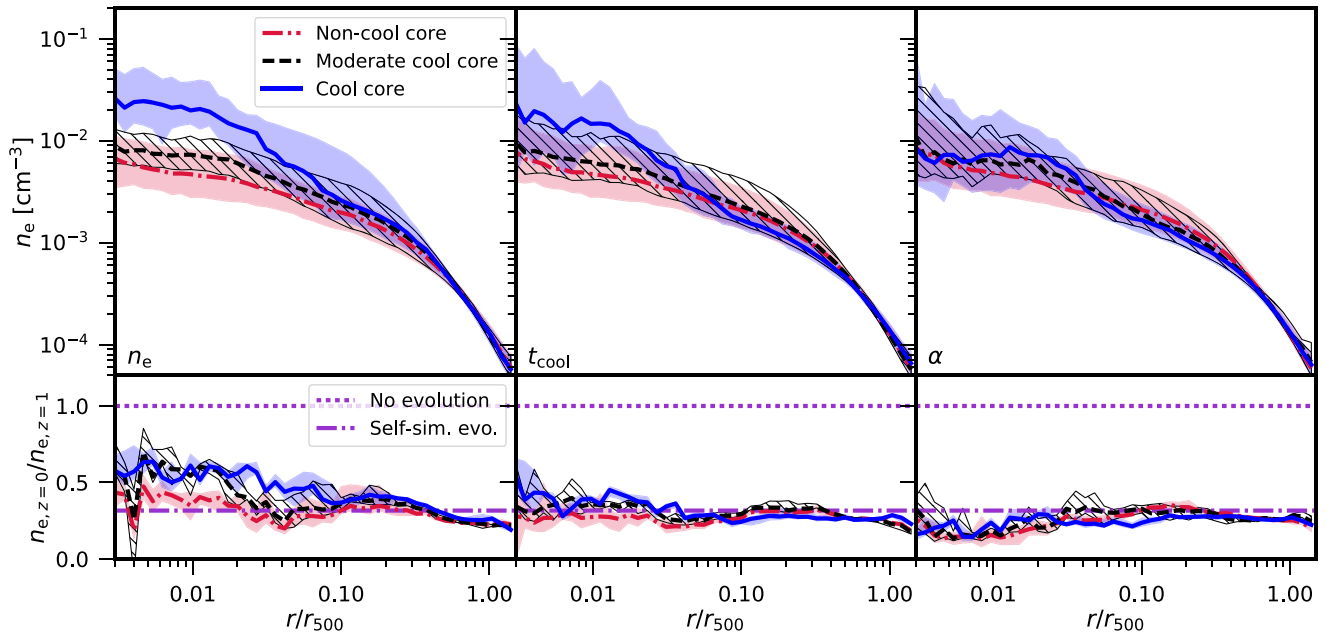


**Figure 11.** Median electron number density profiles at  $z = 0$  (top row) for clusters that are defined as CC (blue solid line), MCC (dashed black line), and NCC (dash-dotted red line) according to the central electron number density (left-hand panel), cooling time (centre panel), and cuspsiness parameter (right-hand panel). Filled and hatched regions enclose 68 per cent of the sample. In the bottom panels, we plot the ratios of the median profiles at  $z = 0$  and  $z = 1$ , with the purple dotted and dash-dotted lines denoting self-similar and no evolution, respectively. All criteria show at least some evolution, in contrast to the observations that show the core region does not evolve between  $z = 1.5$  and  $z = 0$ .

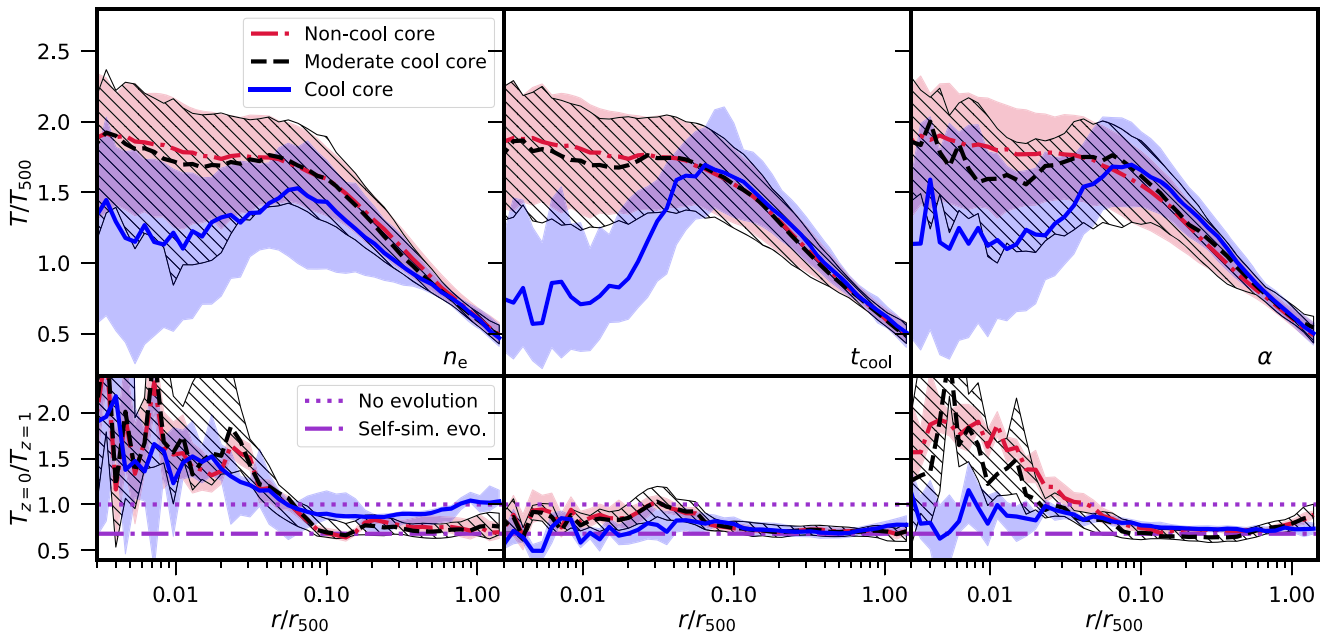


**Figure 12.** Median gas temperature profiles at  $z = 0$  (top row) and the ratio of the median temperature profiles at  $z = 0$  and  $z = 1$  (bottom panel). The line styles are the same as in Fig. 11. For the central electron number density and cuspsiness parameter criteria the temperature in the core of all clusters deviates from the self-similar expectation.

### 6.3 Pressure profiles

In the top row of Fig. 13 we plot the median CC, MCC, and NCC pressure profiles for the different criteria at  $z = 0$ . A linear combination of density and temperature, for  $r > 0.2r_{500}$  the profiles are in good agreement for all criteria, as expected from the density and temperature profiles. Inside this radius the classification of CCs

by the central electron number density yields a CC profile with a central pressure that is 30 per cent larger than the MCC profile, a result of the increased central density. For the central cooling time and cuspsiness parameter the decrease in central temperature offsets the modest increase in central density and all profiles have similar central pressures. The overall change in the normalization of the median CC profiles for the different criteria is due to the mass de-

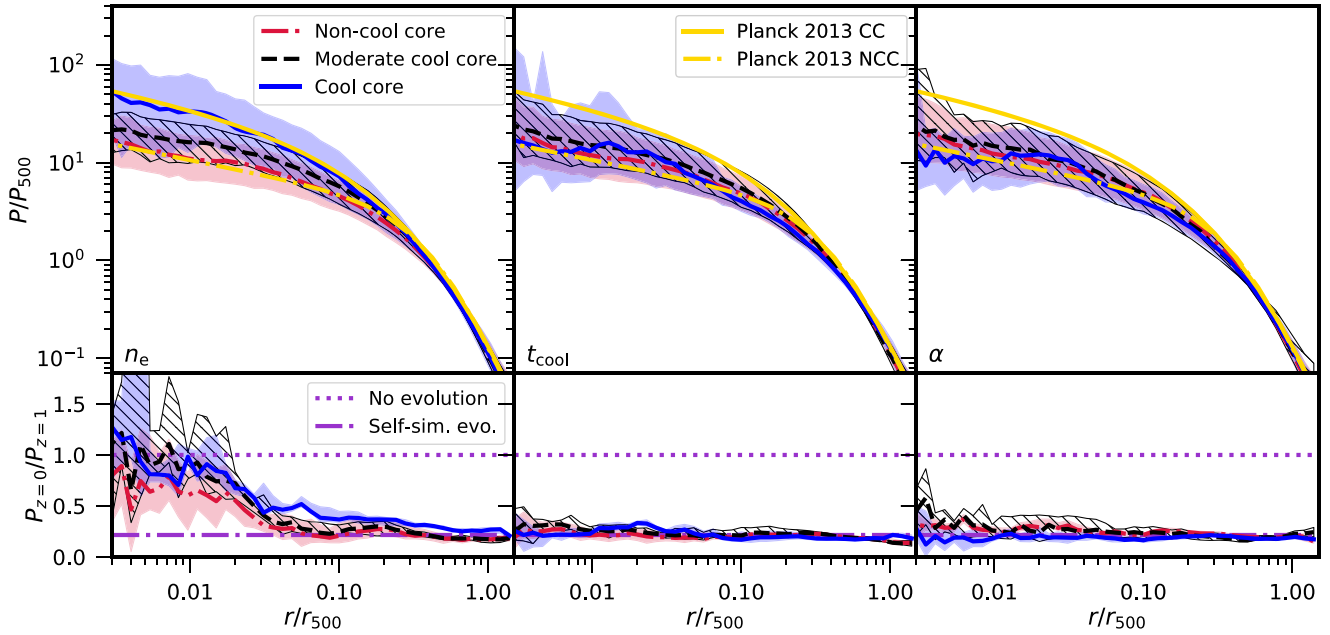


**Figure 13.** Median gas pressure profiles at  $z = 0$  (top row) and the ratio of median pressure profiles at  $z = 0$  and  $z = 1$  (bottom row). The line styles are the same as in Fig. 11. We plot the observed universal pressure profile (yellow) for the CC (solid) and NCC (dot-dashed) clusters using the median mass for each simulated sample (Planck Collaboration V 2013). Using the same criterion the observed and simulated profiles show good agreement, but the differing mass dependence of other criteria results in different CC profiles.

pendence of their scatter, which changes the median mass of the sample.

In addition, we plot the CC and NCC universal pressure profiles for the *Planck* ESZ sample (Planck Collaboration V 2013). CCs were defined as having a central electron number density  $n_e > 4 \times 10^{-2} \text{ cm}^{-3}$  (Planck Collaboration XI 2011). We calculate the observed universal profile using the listed parameters in Planck Collaboration V (2013). For each simulated CC, MCC, and NCC profile for each criteria we calculate the characteristic pressure,  $P_{500}$ , using the median mass of the sample. We then calculated the expected  $P(r/r_{500})$  by multiplying the universal pressure profile by  $P_{500}$ . For all criteria the simulated and observed NCC profiles show good agreement. A like-with-like comparison classifying clusters by the central electron number density results in observed and simulated CC profiles that are in good agreement. However, using a different criterion leads to a disagreement between the simulated profile and the universal profile observed for CCs defined by the central electron number density. Hence, the properties of the average CC changes based on the chosen CC criterion.

In the bottom row, we plot the ratio of the median profiles at  $z = 0$  and  $z = 1$ . The self-similar evolution is given by  $1/E^{8/3}(z = 1) = 0.215$ . All profiles for the central cooling time and cuspsiness parameter criteria are consistent with the self-similar expectation throughout the cluster volume. Classifying clusters by the central electron number density yields profiles consistent with the self-similar expectation for  $r > 0.1r_{500}$ . Inside this radius the average cluster profile evolves less than expected, with central values of 0.76, 0.68, and 0.58 at  $0.01r_{500}$  for the median CC, MCC, and NCC profiles, respectively. This deviation is driven by the lack of evolution in both the temperature and density profiles.

#### 6.4 Entropy profiles

We plot the median CC, MCC, and NCC entropy profiles for the different criteria at  $z = 0$  in Fig. 14. For  $r > 0.1r_{500}$  the profiles are

in good agreement with each other for all criteria and asymptote to the non-radiative result at  $0.6r_{500}$  (Voit et al. 2005). Inside  $0.1r_{500}$  the increased density and decreased temperatures of the CC profiles yield a drop in the entropy profile compared to the NCC profiles. The extent of the drop depends on the defining criteria, with central cooling time CC profile a factor of 5 lower than the NCC profile at  $0.01r_{500}$ , but the cuspsiness parameter CC profile is only a factor 2 lower.

The bottom panels show the ratio of the median profiles at  $z = 0$  and  $z = 1$  for the different CC criteria. The expected self-similar entropy evolution is given by  $1/E^{-2/3}(z = 1) = 1.468$ . We find that all profiles produce ratios that are consistent with the self-similar expectation when classifying clusters by their central cooling time, and greater than self-similar in the core of clusters defined by the cuspsiness parameter. The entropy inside  $r = 0.1r_{500}$  increases faster than expected because the clusters increase in temperature between  $z = 1$  and  $z = 0$ .

#### 6.5 Metallicity profiles

Finally, we examine the median metallicity profiles for the different criteria in the top row of Fig. 15. The profiles are normalized to the solar abundances of Anders & Grevesse (1989). Although examined in Vogelsberger et al. (2018), here we examine how the metallicity evolution changes for different CC criteria. Classifying clusters by their central cooling time we find evidence of a core in the CC profile for  $r < 0.1r_{500}$  with a central metallicity that is 25 per cent higher than the MCC and NCC median profiles. The CC and MCC profiles show evidence of a core when defined by the cuspsiness criterion and have marginally higher central metallicities compared to the NCC profile. The profiles are in good agreement throughout the cluster volume when split by their central electron number density, with all of them showing some hints of a core, i.e. they flatten to a constant central metallicity value.

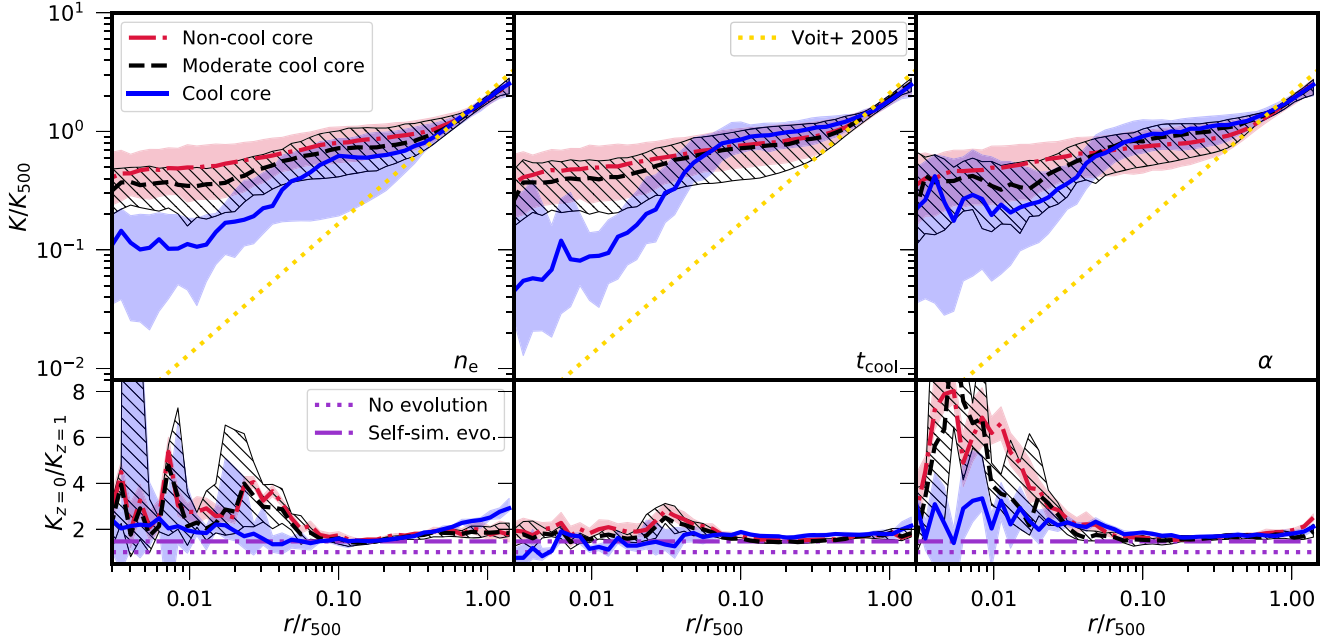


**Figure 14.** Median gas entropy profiles at  $z = 0$  (top row) and the ratio of the median entropy profiles at  $z = 0$  and  $z = 1$  (bottom row). The panels and line styles are the same as in Fig. 11. Additionally, we plot the non-radiative simulations of Voit, Kay & Bryan (2005, yellow dotted) and find that all profiles asymptote to this result at  $0.6r_{500}$ . The entropy profiles between  $z = 1$  and  $z = 0$  increase by at least the self-similar expectation, rising beyond that in the core due to the temperature increase.

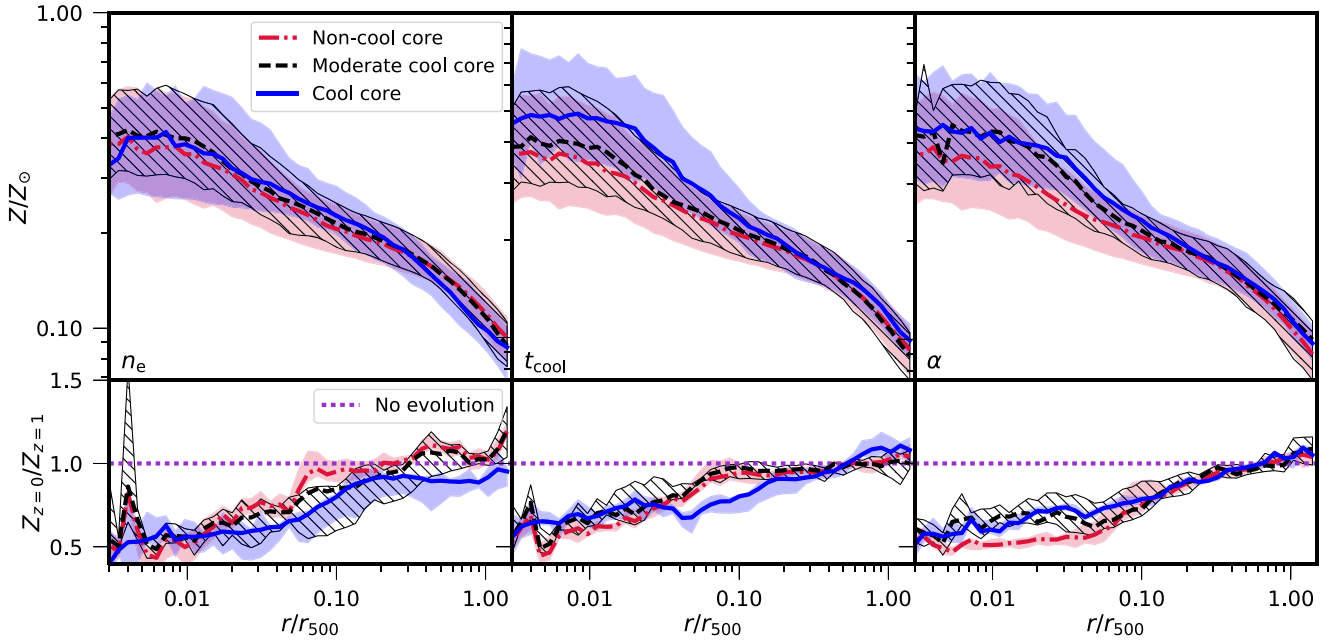


**Figure 15.** Median metallicity profiles at  $z = 0$  (top row) and the ratio of the median metallicity profiles at  $z = 0$  and  $z = 1$  (bottom row). We scale all abundances to the solar values of Anders & Grevesse (1989). The line styles are the same as in Fig. 11. The lack of evolution for  $r > 0.15r_{500}$  is consistent with the idea of early enrichment.

In the bottom row, we plot the ratios of the median profiles at  $z = 0$  and  $z = 1$ . All profiles show the metallicity inside  $0.15r_{500}$  has decreased since  $z = 1$ , a result consistent with previous numerical work (e.g. Martizzi et al. 2016) but inconsistent with the latest observations (e.g. McDonald et al. 2016; Mantz et al. 2017). This may be due to differences in how the subgrid and real AGN shape the ICM and distribute metals or the result of systematic uncertainties

in the observations. Outside the core the profiles are consistent with minimal evolution in the iron abundance and the idea of early enrichment. There are marginal changes in the size of the deficit radius when CCs are classified by different criteria.

In summary, we find that the thermodynamic profiles in the core of simulated clusters have evolved since  $z = 1$ . The extent of this evolution depends on the chosen CC criteria, as the mass depen-

dence of the criterion impacts the median profiles. For example, defining CC via the same criterion as the observed profile yields a good agreement between the simulations and the observations, but differing criteria with opposite mass trends results in differing profiles. The departure of the simulated core profile evolution from the self-similar expectation is in agreement with the observed cluster core evolution, even if the exact scale of the departure differs between the simulations and the observations. Part of this discrepancy, e.g. the reduction in central metallicity, provides insight into how subgrid and real AGN differ in their shaping of the cluster volume. It may also be an indication that additional physical processes, such as anisotropic thermal conduction, must be included to correctly capture the formation and evolution of the cores of clusters.

## 7 CONCLUSIONS

We have examined the fraction of clusters simulated with the IllustrisTNG model that host a CC. We focused on the TNG300 level-1 periodic volume, which has a side length of 302 Mpc and a mass resolution of  $1.1 \times 10^7$  and  $5.9 \times 10^7 M_{\odot}$  for the gas and dark matter components, respectively. We selected all clusters with a mass  $M_{500} > 10^{13.75} M_{\odot}$ , which yielded a sample of 370 (77) clusters at  $z = 0$  ( $z = 1$ ). We then examined the CC fraction for six different criteria commonly used in the literature (Section 4), the evolution of the CC fraction with redshift (Section 5) and how the cluster core evolved in comparison to the rest of the cluster volume (Section 6). Our main results are as follows:

(i) The  $z = 0$  CC fraction for the complete sample is in good agreement with previous numerical work (Rasia et al. 2015; Hahn et al. 2017). Selecting a sample of high-mass clusters we find that the CC fraction at  $z = 0$  decreases for three criteria (central cooling time, central entropy excess, and the cuspsiness parameter) and increases for three criteria (central electron number density and the concentration parameter within physical and scaled apertures) relative to the complete sample. The simulated high-mass sample is lower than the observed CC fraction for four criteria (Fig. 1), and in reasonable agreement for two criteria (central electron number density and the scaled concentration parameter). When fit with a linear relation five criteria are consistent with weak or no mass dependence, with the concentration parameter with scaled apertures the exception. The scatter about the best-fitting relation is mass dependent for the central electron number density and the concentration parameters.

(ii) The simulated gas fractions are lower than observed at  $0.01r_{500}$  and increase more rapidly than observed, with the cumulative profile reaching 86 per cent of the universal fraction at  $0.6r_{500}$  compared to the observed fraction that reaches 83 per cent at  $r_{500}$ . This difference is likely due to the AGN feedback being more violent than in reality, explaining why the simulated CC fractions are lower than observed and some of the differences between the simulated and observed criteria distributions (Fig. 4).

(iii) The simulated central entropy excess distributions are single peaked, but a significant number of the clusters have effectively zero central entropy excess. Previous idealized numerical work and observations of filamentary molecular gas around BCGs support the idea that cold gas precipitates out of the hot phase once the ratio of the cooling time to the free-fall time reaches a small enough value and maintains a minimum central entropy. The simulated central entropy excess distribution may suggest that modelling the formation of a cold phase is an important component in reproducing cluster cores. However, we note that Panagoulia et al. (2014) found

pure power laws entropy profiles if only radii that are sufficiently well resolved are considered, making the exact central profile of CC clusters uncertain.

(iv) The correlations between different CC criteria is mass dependent, with the correlation increasing for more massive systems. For example, the correlation between central electron number density and the cuspsiness parameter improves from  $0.31 \pm 0.06$  for the full sample to  $0.75 \pm 0.10$  when only clusters with  $M_{500} > 2 \times 10^{14} M_{\odot}$  are selected.

(v) Examining the CC fraction as a function of redshift ( Figs 5–9) we find that the high-mass CC fractions are in tentative agreement with the observed CC fractions. However, linear fits to the CC fraction as a function of redshift reveal that the redshift evolution of the CC fraction for the high-mass sample is at least  $2\sigma$  steeper than the observed evolution for the central electron density, the central cooling time and the central entropy. The simulated redshift evolution of the CC fraction defined by the concentration parameter within physical apertures is consistent with the observed evolution, but the normalization is offset at all redshifts. Finally, the redshift evolution of the CC fraction defined by the cuspsiness parameter is poorest fit by a linear relation and the redshift evolution of the simulated sample is consistent with both flat and the negative redshift evolution of the observations. The redshift evolution of the CC fraction for the complete sample is steeper than the high-mass sample for four of the five criteria.

(vi) We found no evidence that the fraction of CCs defined as relaxed is greater than the fraction of NCCs defined as relaxed (Fig. 10). Defining relaxed clusters by the ratio of their kinetic to thermal energy, all samples yield a relaxed fraction that decreases with redshift, consistent with the expectation that the merger rate increases. The result holds for other theoretical definitions of a relaxed cluster. This result seems to be at odds with the idea that mergers solely drive the CC/NCC bi-modality and the observation that radio haloes only occur in NCC clusters.

(vii) Comparing the pressure profiles to the observed universal pressure profile demonstrates that a like-with-like comparison is required. The differing mass dependence of the CC fractions leads to different central pressure profiles and either agreement or disagreement with the observed profile. A like-with-like comparison produces a good agreement between the simulated and observed CC pressure profiles.

(viii) The thermodynamic profiles in the cores of simulated clusters have evolved to some extent between  $z = 1$  and  $z = 0$  ( Figs 11–15), with the extent of the evolution depending on the chosen CC criterion. The simulated core evolution departs from the self-similar expectation for many profiles, with the direction of the departure in agreement with recent observations of the evolution of cluster cores (McDonald et al. 2017). These results indicate that the heating and radiative losses in the centre of the simulated clusters are not in balance in the simulation and point to differences in the way the subgrid AGN and real AGN shape the cluster volume.

We conclude that the IllustrisTNG model matches the observed CC fraction between  $0.25 < z < 1.0$ , but converts CCs to NCCs too rapidly compared to the observations. This results in it overpredicting the fraction of CCs at  $z > 1$  and underpredicting the CC fraction at  $z < 0.25$ . In future work, we will investigate the mechanisms responsible for converting a CC to an NCC as we found that the fraction of CCs and NCCs defined as relaxed were similar, suggesting mergers may not be solely responsible for the dichotomy and in tension with previous numerical work (e.g. Hahn et al. 2017). It seems that subgrid models must continue to de-

velop, especially for the treatment of AGN, and continue to include additional physical processes since essentially all numerical simulations, including IllustrisTNG, do not capture the evolution and thermodynamic profiles of clusters correctly. These physical processes include the impact of cosmic rays (Pfrommer et al. 2017), anisotropic thermal conduction (Kannan et al. 2016, 2017; Barnes et al. 2018), outflows due to radiation pressure from the AGN (Costa et al. 2018a,b), the formation of dust (McKinnon, Torrey & Vogelsberger 2016, Vogelsberger et al. in preparation) and, as simulations push to higher resolution, most importantly more accurate modelling of the interaction between the jet and the intracluster medium (English, Hardcastle & Krause 2016; Weinberger et al. 2017b).

## ACKNOWLEDGEMENTS

We thank Adam Mantz for making data available to us. DJB acknowledges support from STFC through grant ST/L000768/1. MV acknowledges support through an MIT RSC award, the support of the Alfred P. Sloan Foundation, and support by NASA ATP grant NNX17AG29G. RK acknowledges support from NASA through Einstein Postdoctoral Fellowship grant number PF7-180163 awarded by the Chandra X-ray Center, which is operated by the Smithsonian Astrophysical Observatory for NASA under contract NAS8-03060. Simulations were run on the Hydra and Draco supercomputers at the Max Planck Computing and Data Facility, on the HazelHen Cray XC40-system at the High Performance Computing Center Stuttgart as part of project GCS-ILLU of the Gauss Centre for Supercomputing (GCS), and on the joint MIT-Harvard computing cluster supported by MKI and FAS. VS, RW, and RP acknowledge support through the European Research Council under ERC-StG grant EXAGAL-308037 and would like to thank the Klaus Tschira Foundation. The Flatiron Institute is supported by the Simons Foundation. SG and PT acknowledge support from NASA through Hubble Fellowship grants *HST*-HF2-51341.001-A and *HST*-HF2-51384.001-A, respectively, awarded by the STScI, which is operated by the Association of Universities for Research in Astronomy, Inc., for NASA, under contract NAS5-26555. JPN acknowledges support of NSF AARF award AST-1402480. The flagship simulations of the IllustrisTNG project used in this work have been run on the HazelHen Cray XC40-system at the High Performance Computing Center Stuttgart as part of project GCS-ILLU of the Gauss Centre for Supercomputing (GCS). Ancillary and test runs of the project were also run on the Stampede supercomputer at TACC/XSEDE (allocation AST140063), at the Hydra and Draco supercomputers at the Max Planck Computing and Data Facility, and on the MIT/Harvard computing facilities supported by FAS and MIT MKI.

## REFERENCES

Anders E., Grevesse N., 1989, *Geochim. Cosmochim. Acta*, 53, 197  
 Andrade-Santos F. et al., 2017, *ApJ*, 843, 76  
 Bahé Y. M. et al., 2017, *MNRAS*, 470, 4186  
 Barnes D. J., Kay S. T., Henson M. A., McCarthy I. G., Schaye J., Jenkins A., 2017a, *MNRAS*, 465, 213  
 Barnes D. J. et al., 2017b, *MNRAS*, 471, 1088  
 Barnes D. J. et al., 2018, *MNRAS*, preprint ([arXiv:1805.04109](https://arxiv.org/abs/1805.04109))  
 Bleem L. E. et al., 2015, *ApJS*, 216, 27  
 Borgani S., Kravtsov A., 2011, *Adv. Sci. Lett.*, 4, 204  
 Burns J. O., Hallman E. J., Gantner B., Motl P. M., Norman M. L., 2008, *ApJ*, 675, 1125  
 Cameron E., 2011, *PASA*, 28, 128  
 Carlberg R. G. et al., 1997, *ApJ*, 485, L13

Cassano R., Ettori S., Giacintucci S., Brunetti G., Markevitch M., Venturi T., Gitti M., 2010, *ApJ*, 721, L82  
 Cavañolo K. W., Donahue M., Voit G. M., Sun M., 2009, *ApJS*, 182, 12  
 Costa T., Rosdahl J., Sijacki D., Haehnelt M., 2018a, *MNRAS*, 473, 4197  
 Costa T., Rosdahl J., Sijacki D., Haehnelt M. G., 2018b, *MNRAS*, 479, 2079  
 Cowie L. L., Binney J., 1977, *ApJ*, 215, 723  
 Crain R. A. et al., 2015, *MNRAS*, 450, 1937  
 Dolag K., Borgani S., Murante G., Springel V., 2009, *MNRAS*, 399, 497  
 Duffy A. R., Schaye J., Kay S. T., Dalla Vecchia C., 2008, *MNRAS*, 390, L64  
 Dutton A. A., Macciò A. V., 2014, *MNRAS*, 441, 3359  
 Eckert D., Ettori S., Molendi S., Vazza F., Paltani S., 2013, *A&A*, 551, A23  
 Eckert D., Molendi S., Paltani S., 2011, *A&A*, 526, A79  
 English W., Hardcastle M. J., Krause M. G. H., 2016, *MNRAS*, 461, 2025  
 Fabian A. C., Nulsen P. E. J., 1977, *MNRAS*, 180, 479  
 Fakhouri O., Ma C.-P., Boylan-Kolchin M., 2010, *MNRAS*, 406, 2267  
 Foster A. R., Ji L., Smith R. K., Brickhouse N. S., 2012, *ApJ*, 756, 128  
 Gaspari M., 2015, *MNRAS*, 451, L60  
 Gaspari M., Ruszkowski M., Sharma P., 2012, *ApJ*, 746, 94  
 Genel S. et al., 2014, *MNRAS*, 445, 175  
 Genel S. et al., 2018, *MNRAS*, 474, 3976  
 Giocoli C., Tormen G., Sheth R. K., 2012, *MNRAS*, 422, 185  
 Hahn O., Martizzi D., Wu H.-Y., Evrard A. E., Teyssier R., Wechsler R. H., 2017, *MNRAS*, 470, 166  
 Hasselfield M. et al., 2013, *J. Cosmol. Astropart. Phys.*, 7, 008  
 Hogan M. T., McNamara B. R., Pulido F., Nulsen P. E. J., Russell H. R., Vantyghe A. N., Edge A. C., Main R. A., 2017, *ApJ*, 837, 51  
 Hudson D. S., Mittal R., Reiprich T. H., Nulsen P. E. J., Andernach H., Sarazin C. L., 2010, *A&A*, 513, A37  
 Ikebe Y. et al., 1997, *ApJ*, 481, 660  
 Kaiser N., 1986, *MNRAS*, 222, 323  
 Kannan R., Springel V., Pakmor R., Marinacci F., Vogelsberger M., 2016, *MNRAS*, 458, 410  
 Kannan R., Vogelsberger M., Pfrommer C., Weinberger R., Springel V., Hernquist L., Puchwein E., Pakmor R., 2017, *ApJ*, 837, L18  
 Kay S. T., da Silva A. C., Aghanim N., Blanchard A., Liddle A. R., Puget J.-L., Sadat R., Thomas P. A., 2007, *MNRAS*, 377, 317  
 Klypin A., Yepes G., Gottlöber S., Prada F., Heß S., 2016, *MNRAS*, 457, 4340  
 Klypin A. A., Trujillo-Gomez S., Primack J., 2011, *ApJ*, 740, 102  
 Kunz M. W., Schekochihin A. A., Cowley S. C., Binney J. J., Sanders J. S., 2011, *MNRAS*, 410, 2446  
 Landry D., Bonamente M., Giles P., Maughan B., Joy M., Murray S., 2013, *MNRAS*, 433, 2790  
 Lea S. M., Silk J., Kellogg E., Murray S., 1973, *ApJ*, 184, L105  
 Le Brun A. M. C., McCarthy I. G., Schaye J., Ponman T. J., 2014, *MNRAS*, 441, 1270  
 Le Brun A. M. C., McCarthy I. G., Schaye J., Ponman T. J., 2017, *MNRAS*, 466, 4442  
 Lewis A. D., Stocke J. T., Buote D. A., 2002, *ApJ*, 573, L13  
 Lin H. W., McDonald M., Benson B., Miller E., 2015, *ApJ*, 802, 34  
 Li Y., Bryan G. L., 2014, *ApJ*, 789, 153  
 Li Y., Bryan G. L., Ruszkowski M., Voit G. M., O’Shea B. W., Donahue M., 2015, *ApJ*, 811, 73  
 Mantz A. B., Allen S. W., Morris R. G., Schmidt R. W., von der Linden A., Urban O., 2015, *MNRAS*, 449, 199  
 Mantz A. B., Allen S. W., Morris R. G., Simionescu A., Urban O., Werner N., Zhuravleva I., 2017, *MNRAS*, 472, 2877  
 Marinacci F. et al., 2018, *MNRAS*, 480, 5113  
 Martizzi D., Hahn O., Wu H.-Y., Evrard A. E., Teyssier R., Wechsler R. H., 2016, *MNRAS*, 459, 4408  
 Mathews W. G., Bregman J. N., 1978, *ApJ*, 224, 308  
 Maughan B. J., Giles P. A., Randall S. W., Jones C., Forman W. R., 2012, *MNRAS*, 421, 1583  
 McBride J., Fakhouri O., Ma C.-P., 2009, *MNRAS*, 398, 1858  
 McCarthy I. G., Babul A., Bower R. G., Balogh M. L., 2008, *MNRAS*, 386, 1309  
 McCourt M., Sharma P., Quataert E., Parrish I. J., 2012, *MNRAS*, 419, 3319

McDonald M., Veilleux S., Mushotzky R., 2011, *ApJ*, 731, 33  
 McDonald M., Veilleux S., Rupke D. S. N., Mushotzky R., 2010, *ApJ*, 721, 1262  
 McDonald M. et al., 2013, *ApJ*, 774, 23  
 McDonald M. et al., 2014, *ApJ*, 794, 67  
 McDonald M. et al., 2016, *ApJ*, 826, 124  
 McDonald M. et al., 2017, *ApJ*, 843, 28  
 McKinnon R., Torrey P., Vogelsberger M., 2016, *MNRAS*, 457, 3775  
 Molendi S., Pizzolato F., 2001, *ApJ*, 560, 194  
 Naiman J. P. et al., 2018, *MNRAS*, 477, 1206  
 Nelson D. et al., 2018, *MNRAS*, 475, 624  
 Neto A. F. et al., 2007, *MNRAS*, 381, 1450  
 Nurgaliev D. et al., 2017, *ApJ*, 841, 5  
 Pakmor R., Springel V., 2013, *MNRAS*, 432, 176  
 Pakmor R., Springel V., Bauer A., Mocz P., Munoz D. J., Ohlmann S. T., Schaal K., Zhu C., 2016, *MNRAS*, 455, 1134  
 Panagoulia E. K., Fabian A. C., Sanders J. S., 2014, *MNRAS*, 438, 2341  
 Peres C. B., Fabian A. C., Edge A. C., Allen S. W., Johnstone R. M., White D. A., 1998, *MNRAS*, 298, 416  
 Peterson J. R., Kahn S. M., Paerels F. B. S., Kaastra J. S., Tamura T., Bleeker J. A. M., Ferrigno C., Jernigan J. G., 2003, *ApJ*, 590, 207  
 Pfrommer C., Pakmor R., Schaal K., Simpson C. M., Springel V., 2017, *MNRAS*, 465, 4500  
 Pillepich A. et al., 2018a, *MNRAS*, 473, 4077  
 Pillepich A. et al., 2018b, *MNRAS*, 475, 648  
 Pipino A., Pierpaoli E., 2010, *MNRAS*, 404, 1603  
 Planck Collaboration V., 2013, *A&A*, 550, A131  
 Planck Collaboration XI, 2011, *A&A*, 536, A11  
 Planck Collaboration XIII, 2016, *A&A*, 594, A13  
 Planck Collaboration XXVII, 2016, *A&A*, 594, A27  
 Poole G. B., Babul A., McCarthy I. G., Sanderson A. J. R., Fardal M. A., 2008, *MNRAS*, 391, 1163  
 Pratt G. W. et al., 2010, *A&A*, 511, A85  
 Rasia E. et al., 2015, *ApJ*, 813, L17  
 Rossetti M., Gastaldello F., Eckert D., Della Torre M., Pantiri G., Cazzoletti P., Molendi S., 2017, *MNRAS*, 468, 1917  
 Santos J. S., Rosati P., Tozzi P., Böhringer H., Ettori S., Bignamini A., 2008, *A&A*, 483, 35  
 Santos J. S., Tozzi P., Rosati P., Böhringer H., 2010, *A&A*, 521, A64  
 Schaye J. et al., 2015, *MNRAS*, 446, 521  
 Sharma P., McCourt M., Quataert E., Parrish I. J., 2012, *MNRAS*, 420, 3174  
 Sijacki D., Vogelsberger M., Genel S., Springel V., Torrey P., Snyder G. F., Nelson D., Hernquist L., 2015, *MNRAS*, 452, 575  
 Smith R. K., Brickhouse N. S., Liedahl D. A., Raymond J. C., 2001, *ApJ*, 556, L91

Springel V., 2010, *MNRAS*, 401, 791  
 Springel V., White S. D. M., Tormen G., Kauffmann G., 2001, *MNRAS*, 328, 726  
 Springel V. et al., 2018, *MNRAS*, 475, 676  
 Stanek R., Rasia E., Evrard A. E., Pearce F., Gazzola L., 2010, *ApJ*, 715, 1508  
 Suess K. A., Bezanson R., Spilker J. S., Kriek M., Greene J. E., Feldmann R., Hunt Q., Narayanan D., 2017, *ApJ*, 846, L14  
 Torrey P., Vogelsberger M., Genel S., Sijacki D., Springel V., Hernquist L., 2014, *MNRAS*, 438, 1985  
 Tremblay G. R. et al., 2015, *MNRAS*, 451, 3768  
 Vikhlinin A., Burenin R., Forman W. R., Jones C., Hornstrup A., Murray S. S., Quintana H., 2007, in Böhringer H., Pratt G. W., Finoguenov A., Schuecker P., eds, *Heating versus Cooling in Galaxies and Clusters of Galaxies*. Springer-Verlag, Berlin, p. 48  
 Vikhlinin A., Markevitch M., Murray S. S., Jones C., Forman W., Van Speybroeck L., 2005, *ApJ*, 628, 655  
 Vikhlinin A. et al., 2009a, *ApJ*, 692, 1033  
 Vikhlinin A. et al., 2009b, *ApJ*, 692, 1060  
 Vogelsberger M., Genel S., Sijacki D., Torrey P., Springel V., Hernquist L., 2013, *MNRAS*, 436, 3031  
 Vogelsberger M. et al., 2014a, *MNRAS*, 444, 1518  
 Vogelsberger M. et al., 2014b, *Nature*, 509, 177  
 Vogelsberger M. et al., 2018, *MNRAS*, 474, 2073  
 Voit G. M., Kay S. T., Bryan G. L., 2005, *MNRAS*, 364, 909  
 Weinberger R., Ehlert K., Pfrommer C., Pakmor R., Springel V., 2017b, *MNRAS*, 470, 4530  
 Weinberger R. et al., 2017a, *MNRAS*, 465, 3291  
 Werner N. et al., 2014, *MNRAS*, 439, 2291  
 White D. A., Jones C., Forman W., 1997, *MNRAS*, 292, 419  
 Zhuravleva I. et al., 2014, *Nature*, 515, 85

## APPENDIX A: IMPACT OF RESOLUTION ON COOL-CORE CRITERIA

To examine the impact of numerical resolution on the CC criteria distributions we examine the  $z = 0$  clusters in the TNG300 volume at the level 1 and level 2 resolutions. In the left-hand panel of Fig. A1, we plot the fractional difference in the median value of the 6 CC criteria used throughout this work. With the exception of the central entropy excess the median CC criteria values are consistent with each other. In the right-hand panel, we compare the median electron number density and pressure profiles from

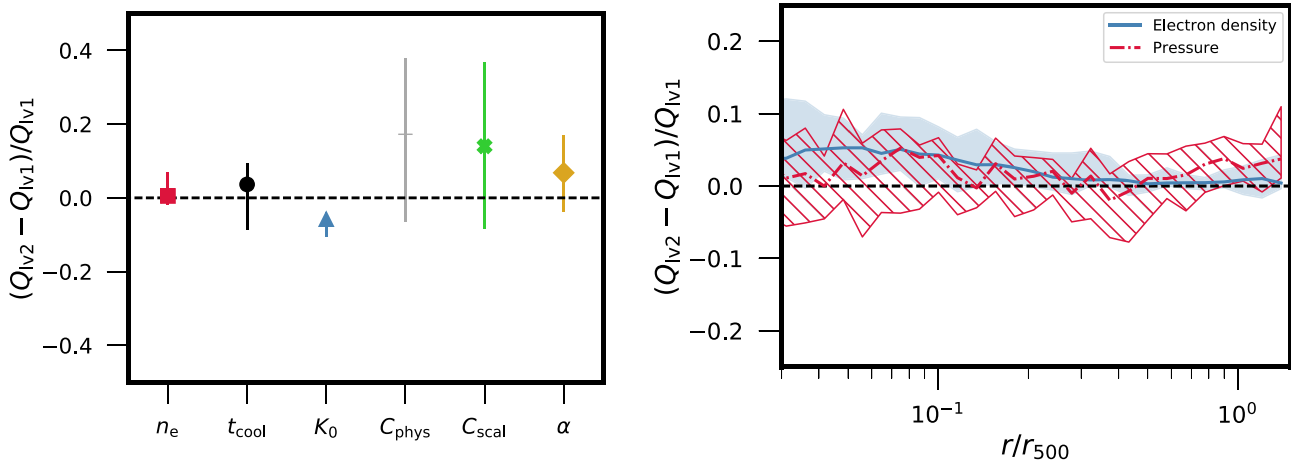


**Figure A1.** Fractional difference in the median CC properties (left-hand panel) and the median electron density (blue) and pressure (red) profiles (right-hand panel) at  $z = 0$  between the level 1 and level 2 resolutions of the TNG300 simulation. The uncertainty is calculated by bootstrapping the samples 10 000 times. With the exception of the central entropy excess the properties are consistent within the errors.

**Table B1.** Correlation and scatter about the best-fitting power law for the different CC criteria at  $z = 0$  for the high-mass sample. The Spearman rank correlation coefficients,  $r_s$ , are shown in the lower off-diagonal entries and the scatter,  $\sigma_{\log_{10}}$ , in the upper off-diagonal entries. Errors are computed by bootstrap resampling 10 000 times.

Criterion	$n_e$	$t_{\text{cool}}$	$K_0$	$C_{\text{phys}}$	$C_{\text{scal}}$	$\alpha$
$n_e$	–	$0.14 \pm 0.05$	$0.22 \pm 0.05$	$0.18 \pm 0.03$	$0.29 \pm 0.09$	$0.33 \pm 0.04$
$t_{\text{cool}}$	$0.98 \pm 0.01$	–	$0.12 \pm 0.02$	$0.36 \pm 0.16$	$0.47 \pm 0.20$	$0.33 \pm 0.06$
$K_0$	$0.94 \pm 0.02$	$0.97 \pm 0.02$	–	$0.40 \pm 0.18$	$0.48 \pm 0.19$	$0.27 \pm 0.05$
$C_{\text{phys}}$	$0.93 \pm 0.02$	$0.94 \pm 0.02$	$0.93 \pm 0.01$	–	$0.14 \pm 0.02$	$0.25 \pm 0.03$
$C_{\text{scal}}$	$0.89 \pm 0.06$	$0.85 \pm 0.08$	$0.81 \pm 0.07$	$0.91 \pm 0.03$	–	$0.20 \pm 0.02$
$\alpha$	$0.75 \pm 0.10$	$0.80 \pm 0.08$	$0.84 \pm 0.06$	$0.72 \pm 0.10$	$0.54 \pm 0.15$	–

the level 1 and level 2 resolutions TNG300 volume. The pressure profiles are consistent with each other within the errors at all redshifts. The electron number density profiles are consistent for  $r/r_{500} > 0.1$ . Inside of this radius we find that the high-resolution simulation has a central electron number density that is 5 per cent larger than the lower resolution simulation, but the uncertainty in the profile is of a similar magnitude. Therefore, we conclude that the results presented in this paper are relatively insensitive to numerical resolution.

## APPENDIX B: HIGH-MASS SAMPLE CORRELATIONS AND SCATTER

In Table B1, we plot the correlation coefficients and the scatter between the different CC criteria considered in this work for the high-mass sample, an analogue to Table 3 for the complete sample.

## APPENDIX C: RELAXED FRACTIONS AND RELAXATION CRITERIA

In Fig. 10, we demonstrated that the fraction of CCs defined as relaxed was consistent with the fraction of NCC clusters and complete sample defined as relaxed. In Fig. C1, we plot the fraction of clusters defined as relaxed by different theoretical criteria, the fraction of mass in substructures,  $F_{\text{sub}}$ , and the offset between the centre of mass and the potential minimum scaled by the  $r_{500}$ ,  $X_{\text{off}}$ . Clusters are defined as relaxed if both  $F_{\text{sub}} < 0.1$  and  $X_{\text{off}} < 0.07$  (Neto et al. 2007). The overall fraction of clusters defined as relaxed has increased, however this can be reduced by making the relatively arbitrary threshold for relaxation stricter. In common with the relaxation criterion presented in Section 5, we find that the relaxed fraction decreases with redshift for all samples and, more importantly, that the fraction of CC clusters defined relaxed is consistent with the fraction of the complete sample and NCC clusters defined as relaxed, regardless of the chosen CC criteria.

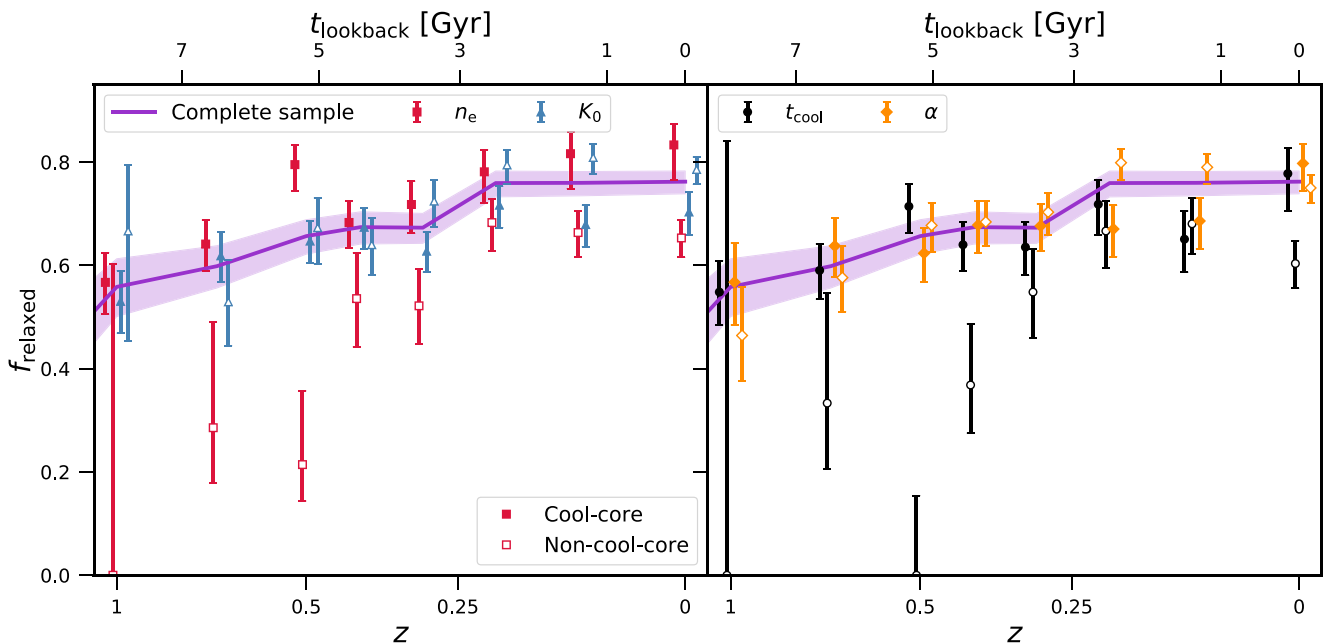


**Figure C1.** Fraction of clusters defined as relaxed via the combination of substructure mass fraction and the offset between the centre of mass and potential minimum as a function of redshift. The line and marker styles are the same as in Fig. 10. The change of relaxation criteria does not impact the result that the complete sample, CC clusters and NCC clusters all have consistent relaxed fractions, regardless of CC definition.